UNIVERSITÀ DEGLI STUDI DI PADOVA

Dipartimento di Fisica e Astronomia "Galileo Galilei"

Master Degree in Physics

Final Dissertation

Tests of gravity with intensity mapping from the Dark Ages

Thesis supervisor

Prof. Alvise Raccanelli

Thesis co-supervisor

Eleonora Vanzan

Candidate

Elena Vanetti

Academic Year 2021/2022

Abstract

This work investigates the potential for testing models of gravity with intensity mapping experiments observing the cosmic Dark Ages. Fluctuations in the brightness temperature of the 21 cm line of neutral hydrogen allow to reconstruct the HI distribution and trace the growth of structures across a wide range of scales and redshifts, for the most part yet to be explored. Observations at high redshifts $z \sim 30 - 200$, however challenging, present numerous advantages and are in principle a high precision cosmological probe. Indeed, the growth of overdensities is still well described by linear perturbation theory and neutral hydrogen can be considered as an unbiased tracer of the underlying matter distribution, furthermore the signal is free of complications due to hard-to-model astrophysical processes. All of this makes it possible to give an analytical description of the signal and isolate the cosmological information.

This thesis aims to generalize existing works on intensity mapping forecasts and develop a formalism and code to compute the angular power spectrum of 21 cm fluctuations during the Dark Ages and constrain the growth of structure. We produce forecasts for the ability of future ground-based radio interferometers, as well as predictions for the proposed radio array on the far side of the Moon, to constrain models of gravity.

Contents

Chapter 1

Introduction to cosmology

Research in cosmology, so far, has led to the formulation of a standard cosmological model, denominated ΛCDM, which provides us with a good understanding of the geometry, components and evolution of the background universe. This concordance model is based on the *cosmological principle*, which states that the universe is homogeneous and isotropic on large scales (> 100 Mpc). Isotropy implies that there is no preferred direction and it's verifiable with observations. Homogeneity, instead, needs to be assumed since we are able to make observations only from the Solar System, but it makes logical sense that we are not a privileged observer.

The universe is currently undergoing a phase of accelerated expansion, as confirmed by many different probes. All observational data is consistent with acceleration being provided by a cosmological constant Λ, or equivalently by an exotic fluid of negative pressure denominated dark energy (DE).

In cosmology, standard particle fields are classified as either radiation or matter, to indicate whether they are relativistic or non-relativistic. According to observations matter constitutes 31% of the total energy density of the present day universe, however, standard baryonic matter can account for only 5% and the radiation fraction is negligible. The remaining components are not part of the Standard Model of particle physics and a lot of ongoing research is focused on understanding their nature. These are non-baryonic cold dark matter (CDM) and the cosmological constant Λ, from which the ΛCDM model takes its name. They constitute 26% and 69% of the total energy density, respectively.

In the last few decades, cosmology has entered a precision era with observations of the Cosmic microwave background (CMB) [1] and the study of the large scale structures (LSS) of the Universe, mainly with galaxy surveys [2, 3]. Thanks to these probes, we achieved measurements of the free parameters of the ΛCDM model around the 1% precision level or better and provided stringent constraints on possible deviations from it.

Despite having passed all observational tests so far, the ΛCDM model still lacks to provide a physical explanation for its main components (dark matter and dark energy) and there is growing tension between early and late measurements of some of its parameters. These fundamental questions remain open and motivate the study of new physics beyond the Standard Model or beyond Einstein's theory of gravity.

In this chapter we give a description of the standard cosmological model and introduce some useful concepts regularly employed in cosmology. Finally, we elaborate further on cosmic acceleration and its origin. We use natural units ($c, \hbar = 1$).

1.1 Geometry and evolution of the background universe

According to the theory of General Relativity (GR), the geometry of spacetime is describes by the metric tensor $g_{\mu\nu}$. Distances are defined by the metric trough the line element

$$ds^2 = g_{\mu\nu}(x)\, dx^\mu\, dx^\nu \tag{1.1}$$

which is invariant under arbitrary transformations of the coordinates x^μ. The equations of motion describing the evolution of the metric are derived from the action

$$S = \frac{1}{2\,\kappa^2}\int d^4x\,\sqrt{-g}\,R\;+\int d^4x\;\mathcal{L}_m \tag{1.2}$$

which is the sum of the Einstein-Hillbert action, describing the gravitational sector, and the action for the matter content of the universe. Here g stands for the determinant of the metric and κ^2 is a positive constant.

The variation of the action above with respect to the metric leads to 10 independent equations of motion: the Einstein equations

$$G_{\mu\nu} = \kappa^2\,T_{\mu\nu} \tag{1.3}$$

The Einstein tensor $G_{\mu\nu} = R_{\mu\nu} - \frac{1}{2}R\,g_{\mu\nu}$, containing second derivatives of the metric, encodes the evolution of the geometry, while the energy-momentum tensor $T_{\mu\nu}$ describes the matter source and it is defined from the variation of the matter Lagrangian density as

$$T_{\mu\nu} = -\frac{2}{\sqrt{-g}}\,\frac{\delta\mathcal{L}_m}{\delta g^{\mu\nu}} \tag{1.4}$$

From the requirement that Newtonian gravity is recovered in the non relativistic and weak field limit, we find the expression for the constant factor $\kappa^2 = \frac{8\pi G}{c^4}$, where G is Newton's constant of gravitation.

1.1.1 The Friedmann equations

A spacially homogeneous and isotropic spacetime is described by the Friedmann–Lemaître–Robertson–Walker metric

$$ds^2 = -dt^2 + a(t)^2\left(\frac{dr^2}{1-k\,r^2} + r^2 d\theta^2 + r^2 sin^2\theta\,d\phi^2\right) \tag{1.5}$$

where we used the signature $(-,+,+,+)$ for the Minkowski metric. The t coordinate is the proper time of the comoving observer, referred to cosmic time, while (r,θ,ϕ) are the spherical comoving coordinates. The scale factor $a(t)$ describes the volume expansion in time and determines the relation between physical and comoving spacial distances $r_{phys} = a(t)r$. Comoving distances, meaning the separation between two fixed comoving coordinates, remain constant by definition, while physical distances increase with the expansion. In this work we adopt the normalization $a_0 = 1$ for the scale factor at present time. The sign of the curvature parameter k determines the curvature of spacial hypersurfaces, which are hyperbolic for negative k, euclidean for $k = 0$ and spherical for positive k. These equivalence classes correspond to an open, flat or closed universe respectively.

The energy-momentum tensor in the homogeneous and isotropic FLRW universe takes the following form in the comoving frame

$$T^\mu{}_\nu = diag(-\rho, P, P, P) \tag{1.6}$$

where ρ and P are the energy density and pressure to which the various constituents of the universe contribute. This is the energy-momentum tensor for a perfect fluid in the reference frame comoving with it, where the 4-velocity is $u^\mu = \delta^\mu_0$. A more general expression, valid for an arbitrary reference frame, is

$$T^{\mu\nu} = (\rho + P)\,u^\mu u^\nu + P\,g^{\mu\nu} \tag{1.7}$$

The Einstein equations for an isotropic and homogeneous universe, described by the FLRW metric, reduce to the Friedmann equations

$$H^2 = \frac{8\pi G}{3}\rho - \frac{k}{a^2} \tag{1.8}$$

$$\frac{\ddot{a}}{a} = -\frac{4\pi G}{3}\;(\rho + 3\,P) \tag{1.9}$$

The dot indicates a partial derivative with respect to cosmic time. The Hubble parameter $H = \frac{\dot{a}}{a}$ describes the volume expansion rate of the universe.

In a FLRW universe the energy-momentum conservation law $\nabla_\nu T^{\mu\nu} = 0$ leads to the continuity equation

$$\dot{\rho} + 3H(\rho + P) = 0 \tag{1.10}$$

However, this equation is not independent from (1.8) and (1.9), since it can also be derived from a combination of the two. In order to solve the system for a, ρ and P we need to employ the equation of state of the fluid

$$P = w\rho \tag{1.11}$$

which provides a third independent equation. The equation of state is $P_r = 1/3\,\rho_r$ for radiation and $P_m \simeq 0$ for matter, which has negligible pressure. The cosmological constant is equivalent to a fluid component with negative pressure $P = -\rho$.

It is useful to define a *critical density* corresponding to the total energy density in a flat universe ($k = 0$)

$$\rho_{crit} = \frac{3H^2}{8\pi G} \tag{1.12}$$

Expressing the energy density of each component in units of ρ_{crit} with the density parameter $\Omega = \rho/\rho_{crit}$, equation (1.8) becomes

$$\Omega + \Omega_k = 1 \tag{1.13}$$

where $\Omega_k \equiv -\frac{k}{a^2H^2}$ is the curvature energy density and $\Omega = \sum_i \Omega_i$ is the sum of the energy density contribution from each fluid component. The most stringent constraints on the density parameters come from the CMB and Baryon Acoustic Oscillations (BAO) data combined [1]:

$$\begin{aligned}\Omega_{m,0} &= 0.3111 \pm 0.0056\\ \Omega_\Lambda &= 0.6889 \pm 0.0056\\ \Omega_{k,0} &= 0.0007 \pm 0.0019\end{aligned}$$

The radiation density today is of the order of $\Omega_{r,0} \sim 10^{-5}$, so it is negligible. From these results we deduce that our universe has negligible spacial curvature but we are unable to determine whether it is open or closed. The ΛCDM model assumes a spacially flat universe, which is a good approximation given that we measured $|\Omega_{k,0}| < 0.0019$, even if this configuration has zero probability. We set $k = 0$ from now on.

The solution to the continuity equation (1.10) for a generic time-dependent equation of state parameter $w(a)$ is

$$\rho(t) = \rho_0\, exp\left(3\int_a^1 \frac{da'}{a'}\left[1 + w(a')\right]\right) \tag{1.14}$$

If we assume w to be constant the solution becomes

$$\rho(t) \propto a^{-3(1+w)} \tag{1.15}$$

and substituting this expression in (1.8), we find the time evolution of the scale factor

$$\begin{aligned}&a \propto t^{\frac{2}{3(1+w)}} && \text{for } w \neq -1\\ &a \propto e^{H\,t}\ ,\ H = \text{const} && \text{for } w = -1\end{aligned} \tag{1.16}$$

The different constituents of the universe are classified based on their equation of state parameter. Below is a summary of the evolution of the energy density of each fluid component and the evolution of the scale factor when such component dominates the energy budget

Matter	$w = 0$	$\rho_m \propto a^{-3}$	$a \propto t^{2/3}$
Radiation	$w = 1/3$	$\rho_r \propto a^{-3}$	$a \propto t^{1/2}$
Λ	$w = -1$	$\rho_\Lambda = \text{const}$	$a \propto e^{H\,t}$

The energy density of each fluid component evolves differently with the scale factor, therefore they dominate the total energy budget at different epochs. The universe initially went trough a radiation-dominated phase, followed by a matter dominated epoch. The transition between the two, defined from the matter-radiation equality condition $\rho_m = \rho_{rad}$, happens at $z_{eq} \simeq 3400$. The dark energy component became dominant only recently at $z \simeq 0.03$, defined from $\rho_\Lambda = \rho_m$.

Equation (1.8) can be expressed in terms of the density parameters at present time

$$E(a)^2 = \Omega_{r,0}\; a^{-4} + \Omega_{m,0}\; a^{-3} + \Omega_{k,0}\; a^{-2} + \Omega_{\Lambda,0} \tag{1.17}$$

where $E \equiv H/H_0$ is the dimensionless expansion rate. The Hubble rate evaluated today is usually written as $H_0 = 100\; h$ km s^{-1} Mpc^{-1}, in function of the reduced Hubble constant h.

Another useful relation can be found from (1.12) and (1.15)

$$\rho_i(a) = \Omega_{i,0}\, \rho_{crit,0}\, a^{-3(1+w_i)} \tag{1.18}$$

from which we see that the measure of the contribution to the energy density budget of the single components constraints the parameter combination $\omega_{i,0} \equiv \Omega_{i,0}\, h^2$. The expression for the matter density contrast then becomes

$$\Omega_m(a) \equiv \frac{\rho_m}{\rho_{crit}} = \frac{8\pi G\, \rho_m}{3\, H^2} = \frac{\Omega_{m(0)}\, a^{-3}}{E^2(a)} \tag{1.19}$$

where in the last passage we used $\rho_m \propto a^{-3}$ and $\rho_{crit} \propto H^2$

1.2 Redshift and distances

Apart from the recent developments in gravitational wave astronomy, our knowledge of the universe is based on the observation of light emitted from distant sources. While light travels, its wavelength is stretched with the expansion as $\lambda \propto a$. This is consistent with the result $E \propto a^{-1}$, coming from the geodesic motion of massless particles in a FLRW metric, once we consider the relation $E = p = h/\lambda$.

The redshift is defined as the as the fractional wavelength shift between the observed and emitted photons

$$z = \frac{\lambda_{obs} - \lambda_{em}}{\lambda_{em}} = \frac{a_0}{a} - 1 \quad \Longrightarrow \quad 1 + z = \frac{a_0}{a} \tag{1.20}$$

In cosmology the redshift and the scale factor can be used as time variables instead of t.

The comoving radial distance between some source of light and us is

$$\chi(t) = \int_r^0 dr' = \int_t^{t_0} \frac{c\, dt'}{a(t')} = \int_a^1 \frac{c\, da'}{a'^2\, H(a')} = \int_0^z \frac{c\, dz'}{H(z')} \tag{1.21}$$

where we have used the fact that, for a radial null path in the FRLW universe, we have $ds^2 = 0 \;\longrightarrow\; cdt = adr$. At small redshifts, the comoving distance is well approximated by $\chi = z/H_0$, which is the Hubble law, verified in the local universe.

A relevant distance in cosmology is the comoving horizon

$$d_H = \int_0^t \frac{cdt'}{a(t')} = \eta \tag{1.22}$$

which is the maximum distance that light could have travelled since the beginning of the standard FRLW universe, set at $t = 0$. Regions separated by a larger distance haven't been causally connected since $t = 0$. This is also the expression for the conformal time η, defined from $cdt = a\, d\eta$, in which the FRLW line element takes the form $ds^2 = a^2(t)\,[-d\eta^2 + dr^2 + r^2 d\Omega^2\,]$.

Distances cannot be measured directly in cosmology, but need to be deduced by the observed light signals. There are several definitions of distance, depending on the chosen observables.

Angular diameter distance
defined from the angle θ subtended by an object of known physical length D (*standard ruler*), assuming zero curvature and that the angle is small

$$d_A = \frac{D}{\theta} = a\chi$$

Angular luminosity distance
defined from the measured luminosity flux of a source of known absolute luminosity L (*standard candle*)

$$F = \frac{L}{4\pi d_L^2} = \frac{La^2}{4\pi\chi^2} \quad \longrightarrow \quad d_L = \frac{\chi}{a}$$

For the second passage we considered that the energy per unit time passing through a sphere of comoving radius χ decreases by a factor a^2 because both the energy and the rate of arrival of the photons decrease by a factor a in an expanding universe.

The relation between the two is $d_L = (1+z)^2 d_A$, so these definitions coincide in the local universe but diverge with increasing redshift.

1.3 Inhomogeneous universe

The Friedmann equations describe the evolution of the smooth background, however, locally the universe has highly inhomogeneous and anisotropic structure. The large-scale structures that we observe today evolved through gravitational instability from primordial density fluctuations generated by inflation, which at the time of last scattering were of order 10^{-4}.

Given that fluctuations are small in the early universe we can describe their evolution with linear perturbation theory. On large enough scales, perturbations are still in the linear regime today, while on small scales fractional fluctuations grew above order one at some point in cosmic history and the perturbative regime ceased to be valid.

The metric perturbed at first order around the flat FLRW background, in the Newtonian gauge[1], is

$$ds^2 = -[\,1 + 2\,\Psi(\vec{x},t)\,]\,dt^2 + a^2(t)[\,1 - 2\,\Phi(\vec{x},t)\,]\,\delta_{ij}\,dx^i dx^j \tag{1.23}$$

With this gauge choice, the scalar metric perturbations Ψ and Φ coincide with the Bardeen potentials, which are gauge invariant quantities.

Perturbations in the energy-momentum tensor traduce into fractional energy density fluctuations and pressure fluctuations, defined from

$$\rho(\vec{x},t) = \overline{\rho}(t)\,[\,1 + \delta(\vec{x},t)\,] \qquad\qquad P(\vec{x},t) = \overline{P}(t) + \delta P(\vec{x},t) \tag{1.24}$$

and peculiar velocities $\vec{v}(\vec{x},t)$, defined as the difference between the local fluid velocity with respect to the background. We use a bar to indicate the background quantities. In this work we neglect anisotropic stress and consider adiabatic pressure.

[1]The Newtonian or longitudinal gauge corresponds to the choice of vanishing off-diagonal metric perturbations

The evolution of cosmological perturbations is derived from the linearized Boltzmann equations for each component (CDM, baryons, photons, neutrinos) and two independent Einstein equations for the Bardeen potentials. For the scope of this work we are interested in the sub-horizon evolution of matter fluctuations well into the matter-dominated epoch. At this time baryons are decoupled from the photons and follow the dark matter evolution closely, so we can consider the total matter density contrast

$$\delta_m(\vec{x},t) = \frac{\delta\rho_m}{\overline{\rho}_m} = \frac{\delta\rho_{\rm cdm} + \delta\rho_b}{\overline{\rho}_{\rm cdm} + \overline{\rho}_b}$$

In this regime matter density fluctuations satisfy the Poisson equation and the continuity and Euler equation for a pressureless Newtonian fluid

$$\begin{cases} \dot{\delta}_m + \frac{1}{a}\vec{\nabla}\cdot\vec{v} = 0 \\ \dot{\vec{v}} + H\vec{v} = 0 \\ \frac{1}{a^2}\nabla^2\Phi = 4\pi G\,\overline{\rho}_m\,\delta_m \end{cases} \tag{1.25}$$

Here gradients are in comoving coordinates and derivatives are taken with respect to cosmic time. In Fourier space, this system of equations translates into

$$\begin{cases} \dot{\delta}_{m\vec{k}} + ikv_{\vec{k}} = 0 \\ \dot{v}_{\vec{k}} + Hv_{\vec{k}} = 0 \\ k^2\Phi_{\vec{k}} = -4\pi G\,a^2\,\overline{\rho}_m\,\delta_{m\vec{k}} \end{cases} \tag{1.26}$$

where we have used the fact that the velocity field is irrotational in cosmology so in Fourier space we have $\vec{v}_{\vec{k}} = v_{\vec{k}}\,\hat{k}$. This follows from the fact that peculiar velocities decay with the expansion as a^{-1} and there are no sources of turbulence on cosmological scales to sustain the vortical component of the velocity field. Only the peculiar velocity component tangent to the field lines of the gravitational field sourced by matter remains. The Fourier transform of the previously defined quantities are indicated with a $\vec{k}$ subscript.

By substituting the three equations in the system (1.26) into the time derivative of the continuity equation, we find the equation equation for the evolution of matter density fluctuations

$$\ddot{\delta}_{m\vec{k}} + 2H\dot{\delta}_{m\vec{k}} - 4\pi G a^2\overline{\rho}\,\delta_{m\vec{k}} = 0 \tag{1.27}$$

In order to describe the growth of matter perturbations it is useful to define the linear growth rate

$$f \equiv \frac{d\ln\delta}{d\ln a} = \frac{\dot{\delta}}{H\delta} \tag{1.28}$$

Substituting this definition in the continuity equation we find an expression connecting the peculiar velocity gradient to the matter density field, which we report also in Fourier space

$$\vec{\nabla}\cdot\vec{v} = -aHf\delta_m \quad \Longrightarrow \quad v_{\vec{k}} = \frac{ifaH\delta_{m\vec{k}}}{k} \tag{1.29}$$

1.3.1 Statistics

Correlations functions are an important tool in cosmology because it's only possible to predict the average statistical properties of the universe from any given theory. The average needs to be taken over the ensemble of all possible realizations of the underlying cosmological model, however, this is not possible in practice since we have only one universe to observe. This problem is circumvented with the *fair sample hypothesis*, which states that well separated areas of the universe can be considered as independent realizations of the same physical process. Following this reasoning we can replace the ensemble average with a spatial average.

The limit in the number of patches over which the average is performed introduces an uncertainty, called *cosmic variance*, that cannot be removed by improving the sensitivity of the experiment and increases when considering larger scales.

The 2-point correlation function for a generic fluctuation field $\delta(\vec{x}, t)$ is the ensemble average of the product between the field evaluated at two different points in space $\vec{x}_1$ and $\vec{x}_2$ and at the same time

$$\xi(\vec{x}_1, \vec{x}_2, t) = \langle \delta(\vec{x}_1, t)\, \delta^*(\vec{x}_2, t) \rangle \tag{1.30}$$

For a gaussian random field, the full statistical information is encoded in the 2-point function and all higher orders correlations are set to zero. If the field is isotropic, the 2-point correlation function depends only on the modulus of the distance between the two points $\vec{r} \equiv \vec{x}_1 - \vec{x}_2$, so we have $\xi = \xi(r, t)$. We express the time-dependence with redshift from now on.

It can be useful to carry out analyses in Fourier space, where the 2-point statistical information is encoded in the power spectrum $P(k, z)$, defined from the relation

$$\langle \delta^*(\vec{k}_1, z)\, \delta(\vec{k}_2, z) \rangle = (2\pi)^3 \delta^D(\vec{k}_1 - \vec{k}_2) P(k, z) \tag{1.31}$$

$\delta(\vec{k}, z)$ is the Fourier transform of the field and δ^K is the Dirac delta function. In the isotropic case the power spectrum depends only on the modulus of the wavevector $|\vec{k}|$. It's immediate to see that the power spectrum is the Fourier transform of the 2-point correlation function

$$\xi(r, z) = \int \frac{d^3k}{(2\pi)^3} e^{i\vec{k}\cdot\vec{r}} P(k, z) \tag{1.32}$$

The dimensionless power spectrum $\Delta(k) = \frac{k^3}{2\pi^2} P(k)$ is also often used in the literature.

When considering a thin redshift slice centered in z, observables need to be projected on a sphere. In order to do so we expand the field $\delta(\vec{x}, z)$ in spherical harmonics with coefficients $\delta_{\ell m}(z)$ and use the relation $\langle \delta^*_{\ell m} \delta_{\ell' m'} \rangle = \delta^K_{\ell\ell'}\, \delta^K_{mm'}\, C_\ell$ coming from the statistical isotropy requirement, where δ^K is the Kronecker delta. After these passages(1.30) becomes

$$\xi(\hat{n}_1, \hat{n}_2, z) = \langle \delta^*(\hat{n}_1, z) \delta(\hat{n}_2, z) \rangle = \sum_{\ell=0}^{\infty} \frac{2\ell + 1}{4\pi} \mathcal{P}_\ell(\hat{n}_1 \cdot \hat{n}_2) C_\ell(z) \tag{1.33}$$

where P_ℓ is the Legendre polynomial of order ℓ and $\hat{n}$ is the line of sight direction. As a consequence of isotropy, the correlation function depends only on the angular separation between the two directions. The angular power spectrum is

$$C_\ell(z) = \langle \delta^*_{\ell m}(z)\, \delta_{\ell m}(z) \rangle = \frac{2}{\pi} \int dk\, k^2\, P(k, z)\, j^2_\ell(k\, \chi) \tag{1.34}$$

where j_ℓ is the spherical Bessel function of order ℓ and χ is the distance along the line of sight. This is derived starting from the expression for the spherical harmonics coefficients, combined with the Fourier transform of the density field

$$\delta_{\ell m}(z) = \int d\Omega\, Y^*_{\ell m}(\hat{n}) \int \frac{d^3k}{(2\pi)^3} e^{i\vec{x}\cdot\vec{k}}\, \delta(\vec{k}, z) \tag{1.35}$$

For realistic experiments, the finite frequency resolution needs to be taken into account with a window function

$$\delta(\hat{n}, z) = \int_0^\infty d\chi\, W_z(\chi)\, \delta(\hat{n}, \chi) \tag{1.36}$$

The window function $W_z(\chi)$ is typically taken as a top-hat or a gaussian centered at redshift z with width corresponding to the resolution of the experiment.

Introducing anisotropy

Relation (1.34) changes in presence of line of sight effects that introduce anisotropy in the power spectrum. Angular dependence in the power spectrum can be traduced into derivatives of the spherical Bessel functions following the prescription

$$\mu^p e^{i\vec{k}\vec{x}} \quad \longrightarrow \quad (-i)^{(p)} j_\ell^p(k\,\chi) \tag{1.37}$$

where $\mu \equiv \hat{x}\cdot\hat{k}$ is the cosine of the angle between the line of sight and the wave vector of the Fourier mode. For numerical applications it's useful to rewrite the spherical Bessel functions' derivatives following the recurrence relation

$$j'_\ell(x) = \frac{\ell}{2\ell+1} j_{\ell-1}(x) - \frac{\ell+1}{2\ell+1} j_{\ell+1}(x) \tag{1.38}$$

Another possibility is to translate the angular dependence into derivatives of the window function, as detailed in [4], with the prescription

$$\mu\, W_z(\chi) \quad \longrightarrow \quad \frac{-i}{k}\,\frac{\partial W_z(\chi)}{\partial \chi}$$

1.3.2 The matter power spectrum

Statistical information about the distribution of matter and its evolution is contained in the power spectrum of linear matter density fluctuations $P(k,z)$, defined from

$$\langle \delta_m^*(\vec{k},z)\delta_m(\vec{k}',z)\rangle = (2\pi)^3\delta^K(\vec{k}-\vec{k}')\,P(\vec{k},z) \tag{1.39}$$

where $\delta_m(\vec{k},z)$ is the Fourier transform of the total matter density contrast. The matter power spectrum at some redshift z is related to the primordial power spectrum $\mathcal{P}(k)$ generated during inflation through the linear growth factor $D(z)$ and the transfer function $T(k,z)$

$$P(k,z) = D(z)^2\,T(k,z)^2\,k^4\,\mathcal{P}(k) \tag{1.40}$$

The power spectrum of primordial scalar fluctuations can be written as a power law

$$\mathcal{P}(k) = \frac{2\pi^2}{k^3}\,A_s\left(\frac{k}{k_*}\right)^{n_s-1} \tag{1.41}$$

A_s is its amplitude at an arbitrary pivot scale k_*, chosen as $k_* = 0.05$ Mpc^{-1} by convention, and n_s is the primordial scalar spectral index. The scale-dependence of the primordial power spectrum is close to k^{-3}, since $n_s = 0.9649 \pm 0.0044$ (from the Planck TT,TE,EE+lowE data [1].

The linear growth factor is defined as

$$\delta_m(z) = D(z)\,\delta_m(0) \tag{1.42}$$

and accounts for the the scale-independent evolution of matter perturbations. The transfer function contains the scale dependent evolution and it is defined as $T(k) = \Phi(k,z)/\Phi(0,z)$ with z well-into the matter dominated epoch, when the evolution becomes scale-independent The k^4 dependence in (1.40) comes from relating matter density fluctuations to the gravitational potential with the Poisson equation.

The exact solution for the transfer function has to be found numerically by solving the system of Boltzmann and Einstein equations which describes the evolution of cosmological perturbations at linear order. This can be done with publicly available codes like `CLASS` [2] [5]. An analytical fitting formula, reproducing the numerical results with precision below 5%, is provided in [6].

The matter power spectrum has been constrained by numerous independent probes (see Figure 1.1) and measurements of increasing precision on large scales are expected to come with the next generation of galaxy surveys. In the following sections we identify two regimes in the scale-dependence and describe its main features.

[2] http://www.class-code.net

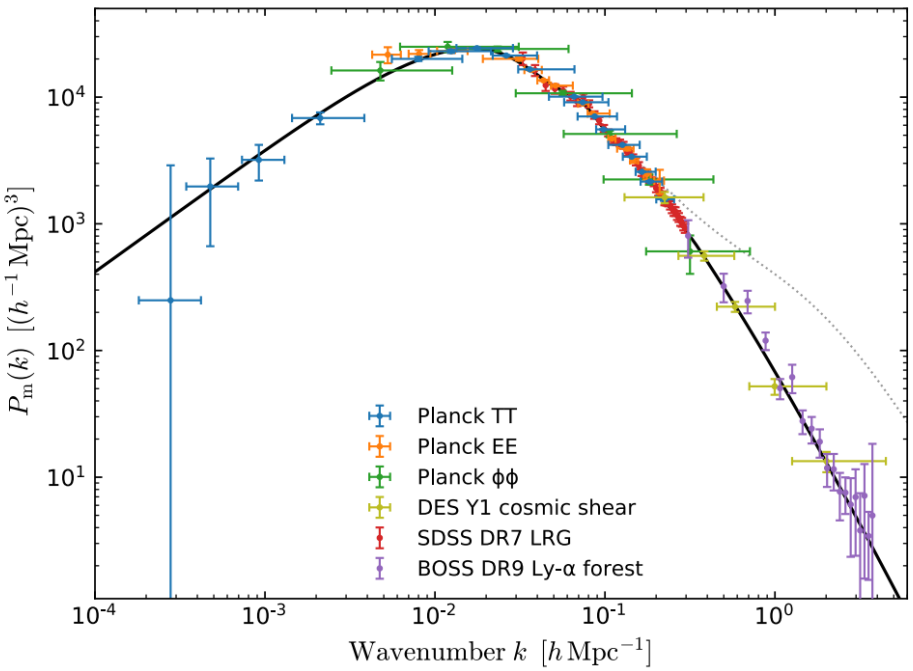

Figure 1.1: Constraints on the linear matter power spectrum at $z = 0$ from different probes and prediction from the ΛCDM model (solid black line). Plot taken from [7]. The dotted gray line is obtained by taking into account non linear evolution on small scales.

Growth of CDM fluctuations

In adiabatic conditions, perturbations stay constant super-horizon, where the power spectrum scales as the primordial one $P \propto k^{n_s-4} \simeq k^{-3}$. On sub-horizon scales, matter perturbations grow differently depending on the dominant component in the energy budget. CDM perturbations grow logarithmically with the scale factor ($\propto \ln a$) during the radiation dominated epoch and linearly ($\propto a$) after matter-radiation equality. The growth slows down again at late times due to the accelerated expansion. In absence of baryons and anisotropic stress, the scale dependence in the growth arises from different modes entering the horizon at different times:

- Modes entering the horizon well before matter-radiation equality ($k \gg k_{eq}$) grow in a scale-independent way during the matter dominated epoch and the power spectrum keeps the scale-dependence gained from the evolution during the radiation epoch $P(k) \propto k^{n_s-4}(\ln k)^2$.

- Modes entering the horizon well into the matter era ($k_\Lambda \ll k \ll k_{eq}$) grow by a quantity $\delta_m(a)/\delta_m(a_{hc}) \simeq a/a_{hc} = (\eta/\eta_{hc})^2 \sim \eta k^2$. In the last two passages we used the fact that the conformal time at horizon crossing is $\eta_{hc} = 1/k$ ad $\eta \propto a^{1/2}$ during matter domination. The power spectrum gains the dependence $P(k) \propto k^{n_s}$ over these scales.

When the cosmological constant becomes the dominant component, the growth slows down while remaining scale-independent, so the shape of the power spectrum on scales already inside the horizon is not affected.

Baryons Acoustic Oscillations

The presence of baryons brings observable changes in the matter power spectrum, even if they constitute only a small fraction of the total matter energy density. Prior to recombination, photons and baryons are coupled by very efficient Compton scattering and behave like a single fluid. Acoustic waves propagate in the baryon-photon fluid with speed $c_s = \frac{1}{\sqrt{3(1+R)}}$, where $R = 3\rho_b/4\rho_\gamma$, until baryons decouple from the photons at t_{dec}. Before decoupling, the sound waves can travel for a comoving

distance

$$r_s(t_{dec}) = \int_0^{t_{dec}} dt \frac{c_s(t)}{a(t)}$$

referred to as the *sound horizon*. This scale remains imprinted in the matter distribution as a peak at $r \sim 100\,h^{-1}$ Mpc in the 2-point correlation function, which traduces into oscillations at $k \gtrsim 0.01\,h$ Mpc^{-1} in the matter power spectrum, known as *baryon acoustic oscillations* (BAO). Acoustic waves propagating in the baryon-photon fluid also leave a series of peaks in the angular power spectrum of the CMB (acoustic peaks).

After decoupling from the photons, baryons fall into the gravitational potential wells created by CDM fluctuations, which were free to grow in the meantime, and soon catch up with the CDM evolution. Therefore we can use the same transfer function for both and consider the evolution of the total matter density. Since baryon fluctuations don't grow before decoupling, the presence of a baryon fraction in the total matter energy density determines a step-like suppression of the power spectrum on scales below the sound horizon, with respect to its amplitude in a cold dark matter only scenario.

The BAO scale provides a standard ruler and, if measured at different redshifts, can be used to reconstruct the expansion history of the background universe. The BAO feature has already been detected with high significance in the galaxy distribution [3].

1.4 Cosmic acceleration

Cosmic acceleration was discovered in 1998 [8], when a negative value for the deceleration parameter $q_0 \equiv -\ddot{a}/aH^2|_{t_0}$ was measured from a sample of 10 type Ia supernovae in the redshift range $0.16 < z < 0.62$. This result was later confirmed by a variety of independent probes, including the CMB, the BAO feature in the matter power spectrum and other measures with standard candles.

The mechanism behind the observed cosmic acceleration is still under discussion and understanding its nature represents one of the main challenges of modern cosmology. Possible explanations currently under research are the presence of an additional matter field (usually a scalar) in the context of GR, deviations from General Relativity on cosmological scales or interaction in the dark sector. No observational signature of any of these theories has been detected so far.

1.4.1 The cosmological constant

The observed accelerated expansion is consistent with a constant term -2Λ added to the Einstein-Hillbert lagrangian, which is not prohibited by its symmetries.

$$S = \frac{1}{2\kappa^2} \int dx^4 \sqrt{-g}\ (R - 2\Lambda) + \int dx^4\ \mathcal{L}_m \tag{1.43}$$

This results in an extra term in the Einstein equations

$$G_{\mu\nu} + \Lambda\, g_{\mu\nu} = \kappa^2\, T_{\mu\nu} \tag{1.44}$$

which can also be interpreted as part of the energy-momentum tensor

$$G_{\mu\nu} = \kappa^2\,(T_{\mu\nu} + T^{(\Lambda)}_{\mu\nu}) \quad \text{with} \quad T^{(\Lambda)}_{\mu\nu} = -\frac{1}{\kappa^2}\Lambda\, g_{\mu\nu} \tag{1.45}$$

For a homogeneous and isotropic universe, this traduces into an extra term $\frac{\Lambda}{3}$ added to both Friedmann equations, which corresponds to an additional effective fluid component (dark energy) with energy density $\rho_\Lambda = \frac{\Lambda}{8\pi G}$ and equation of state parameter $w_\Lambda = -1$ constant at all redshifts.

Distinctive observational features of the cosmological constant are a smooth DE fluid with constant energy density. Measuring a time-varying dark energy equation of state or a signature of dark energy perturbations would exclude this scenario.

Problems with the cosmological constant

Despite being the simplest model to justify the accelerated expansion and being consistent with all observations, the cosmological constant is affected by several issues that cannot be overlooked.

One of the main problems is that there is no theoretical motivation for the small value of Λ that we observe. A possible physical explanation would be that Λ is the vacuum energy contribution from all particle fields, however, the value of Λ predicted from quantum field theory is larger that the measured value by 120 orders of magnitude [9]. This result could either mean that there are some unaccounted-for effects in the calculation, for example a missing prescription for the correct computation of the vacuum contribution or a new component canceling out the vacuum energy very precisely, or that the cosmic acceleration has different origin.

Another issue, generally referred to as the *cosmic coincidence* problem [10, 11], is that at present time we observe an energy density associated with the cosmological constant of the same order of magnitude of the matter energy density, despite their different evolution with the expansion. This requires their ratio in the early universe to be tuned to a specific very small value.

Furthermore, it is to be noted that a cosmological constant cannot be responsible for inflation since the phase of accelerated expansion needs to end for the standard radiation-dominated phase to begin. However, once Λ becomes the dominant component in the energy budget of the universe, it gives rise to a phase of exponential expansion with no end.

1.4.2 Dynamical dark energy

If we exclude the cosmological constant because of the aforementioned problems and assume that General Relativity is correct, the accelerated expansion could be explained by an additional dynamical degree of freedom (d.o.f.), which corresponds to a perfect fluid with a time-varying equation of state parameter $w_{DE}(a)$. At late time this needs to be nearly constant around -1 in order to reproduce observations.

The simplest class of models with these characteristics is *quintessence*, where the additional d.o.f. is a canonical scalar field minimally coupled to gravity with a potential flat enough to undergo a slow-roll phase, in analogy with the well-studied single field inflation models.

An advantage of quintessence is that both inflation and the late time acceleration can be explained within the same model. It is also possible to explain cosmic coincidence with the tracking behavior of the dynamical field, without the need to fine-tune initial conditions [11]. However, quintessence models are still plagued by fine-tuning problems and can be difficult to motivate from a particle physics standpoint because of the very low mass scale that they introduce. In fact, the scalar field needs to have mass $m_\phi \lesssim H_0 \sim 10^{-33}$eV [12] in order to realize the observed accelerated expansion.

1.4.3 Modified gravity

Another possibility to explain the accelerated expansion is that General Relativity is not a good description for gravity on cosmological scales. While GR has been tested to high precision in the Solar System, it's still not very well constrained on large scales, where the possibility of deviations from it is still open.

Modified gravity theory introduce at least one new degree of freedom in the gravitational sector. This traduces into an additional interaction, commonly referred to as the *fifth force*, which should have long range on the background in order to reproduce the cosmic acceleration. The presence of a fifth force implies violation of the strong equivalence principle, while the weak equivalence principle could still be satisfied, provided that the coupling to standard matter fields is universal. Since the presence of an additional interaction is strictly constrained by local gravity experiments, viable modified gravity theories should include some type of screening mechanism for the fifth force acting in high density environments in order to recover GR to high precision in the Solar System.

It is to be noted that the distinction between modified gravity and dark energy models is not straight forward because any modification to the gravitational sector can be interpreted in the equation of motion as an additional component to the energy momentum tensor, in analogy with (1.45), and therefore as a modification of the matter source. Models in which the extra d.o.f affect the other fields only by interacting with them gravitationally according to GR, are generally referred to as standard dark energy scenarios. The strong equivalence principle is not violated in this case. Instead, models that introduce a fifth force and therefore violate the strong equivalence principle are referred to as modified gravity. This includes interacting dark energy.

Chapter 2

21 cm Line Intensity Mapping

To this day, only a small portion of the history of the universe is accessible with direct observations. The CMB lets us observe a small redshift window in the early universe, at $z \sim 1100$. Most galaxy surveys, on the other hand, are confined to the range $0 < z \lesssim 1$ because they target discrete objects and a high threshold on the signal-to-noise ratio is needed in order to distinguish the candidate sources from noise fluctuations. Consequently, galaxy surveys rapidly lose effectiveness with increasing redshift, as sources become more faint.

Line Intensity Mapping (LIM) [13] is an emerging technique in observational cosmology that could give access to higher redshifts and larger scales compared to other probes and therefore allow to test the ΛCDM model with high precision over unexplored epochs. It consists in measuring the integrated emission of atomic or molecular spectral lines originating from individually unresolved galaxies and the diffuse intergalactic medium (IGM). LIM is therefore sensitive to all the sources that emit in the chosen line, giving access to sources that are too faint to be detected individually and thus enabling to probe higher redshifts than galaxy surveys.

Another advantage of using spectral lines is that the frequency at which the line is observed today can be used to deduce the redshift information with high precision, which corresponds to a high resolution on the distance along the line of sight. Precise redshift information combined with the possibility to gather data on a wide range of redshifts allow to perform tomographic analysis with thin redshift bins and reconstruct the evolution of the LIM signal for extended epochs in the history of the universe.

LIM also requires lower resolution, since the single sources don't need to be detected individually. This allows for instruments with a wider instantaneous field of view that can scan large portions of the sky in a short time. As a consequence, LIM surveys are cheaper than current galaxy surveys and able to cover larger volumes. Because of these characteristics, LIM is an optimal technique to track the growth of density perturbations across cosmic time and gives the possibility to improve the constraints on the ΛCDM model parameters and possibly detect deviations from it implying new physics, as discussed in [14] [15].

A number of different spectral lines are relevant in cosmology, among which CO rotational lines, CII fine structure lines [16] and the $Ly\alpha$ and 21 cm line of the hydrogen atom. In this work we consider the 21 cm line (or HI line) emission of neutral hydrogen from the Dark Ages, before the formation of the first stars. During this epoch the baryonic matter content of the universe is constituted mainly of neutral hydrogen and the 21 cm emission is the only tracer of cosmic structure.

Observations at such high redshifts are challenging but they present numerous advantages: during the Dark Ages neutral hydrogen can be considered as an unbiased tracer of the underlying matter distribution and density fluctuations are small enough to be described by perturbation theory on all scales [17], making it possible to give an analytical description of the signal in function of cosmological parameters. Furthermore, while CMB fluctuations are erased by Silk damping below the scale $k_{\text{silk}} \sim 0.15\ \text{Mpc}^{-1}$, fluctuations in the hydrogen distribution can develop down to the Jeans scale

$k_J \sim 300$ Mpc^{-1} after last scattering, allowing to probe smaller scales with respect to the CMB. At last, during the Dark Ages the 21 cm signal has no astrophysical dependence, which is a great advantage since it is often difficult to model astrophysical processes with enough precision to isolate the cosmological information, as discussed in [15].

In this chapter we introduce some concepts about the 21 cm line of neutral hydrogen and we model the 21 cm signal from the Dark Ages, following mainly the references [18], [19] and [20].

2.1 Physics of the 21 cm line

The 21 cm line is the spectral line corresponding to the hyperfine splitting of the 1S ground state of neutral hydrogen into a singlet and triplet state. The transition between the two is known as spin-flip transition. The energy difference between the two states is $E_{21} = 5.9 \times 10^{-6}$eV and corresponds to a wavelength of 21 cm and to a frequency of 1420 MHz. These are well known and precisely measured quantities in physics.

2.1.1 The spin temperature

The signal from 21 cm line transitions can be described in terms of its excitation temperature, which is known as the spin temperature and is defined as follows

$$\frac{n_1}{n_0} = \frac{g_1}{g_0} e^{-T_* / T_s} \tag{2.1}$$

The spin temperature T_s quantifies the relative number density of hydrogen atoms in the two hyperfine levels of the ground state, which here are labeled by the subscript 0 for the 1S singlet state and 1 for the 1S triplet state. $g_0 = 1$ and $g_1 = 3$ are the statistical degeneracy factors of the singlet and triplet state and $T_* \equiv \Delta E_{21}/k_B = 68$ mK is the temperature corresponding to the energy splitting between the two levels. It is important to note that the approximation $T_* \ll T_s$ holds for all cases of astrophysical interest.

The spin temperature is determined by the balance of all the processes causing transitions between the two hyperfine levels. Its expression is derived here following reference [20].

The spontaneous decay rate of the triplet state is given by the Einstein coefficient $A_{10} = 2.85 \times 10^{-15} s^{-1}$, which translates into a lifetime lifetime of $\tau = 11$ Myr. Radiative and collisional transitions due to interactions of the hydrogen atoms with the environment happen on a much smaller timescale and hence drive the evolution of the spin temperature, making this quantity sensitive to the density and thermal state of the intergalactic medium. A brief description of these processes follows:

- **Absorption and induced emission of 21 cm photons**
  The excitation and de-excitation rates due to 21 cm photon absorption and emission can be written as [21]
  $$P_{01} = A_{10} + B_{10} I_\nu \qquad P_{10} = B_{10} I_\nu \tag{2.2}$$
  where I_ν is the specific intensity of the 21 cm radiation and
  $$B_{10} = \frac{c^3}{2h\nu^3} A_{10} \qquad B_{01} = \frac{g_1}{g_0} B_{10} \tag{2.3}$$
  are the appropriate Einstein coefficients.

  Their ratio can be expressed in terms of the brightness temperature of the 21 cm radiation T_R
  $$\frac{P_{01}}{P_{10}} = \frac{A_{10} + B_{10} I_\nu}{B_{10} I_\nu} \simeq 3 \left(1 - \frac{T_*}{T_R}\right) \tag{2.4}$$
  The primary source of 21 cm photons during the Dark Ages is the CMB, so for the rest of this work T_R will be identified with the CMB temperature T_γ. The relations between the Einstein

coefficients and the Rayleigh-Jeans law[1], together with the $T_* \ll T_R$ approximation, were used in the second step.

- **Collisions with H atoms, free electrons and free protons:**
  The ratio between the collisional excitation and de-excitation rates can be derived from detailed balance:
  $$\frac{C_{01}}{C_{10}} = \frac{n_1}{n_0} = 3e^{-T_*/T_k} \simeq 3\left(1 - \frac{T_*}{T_k}\right) \tag{2.5}$$
  where T_k is the kinetic temperature of the neutral hydrogen gas and the $T_* \ll T_k$ approximation was taken at the end.

- **Scattering of Lyα photons**
  Also called Wouthuysen-Field effect, the scattering with UV light can cause a spin-flip transition with an intermediate excited state. The effective color temperature T_α of the UV radiation field is defined as
  $$\frac{P_{01}^{Ly\alpha}}{P_{10}^{Ly\alpha}} \equiv 3\left(1 + \frac{T_*}{T_\alpha}\right) \tag{2.6}$$
  In most situations of interest $T_c = T_k$ is a good approximation, as proved in [20].

The processes mentioned above happen on a timescale smaller than the Hubble time by several orders of magnitude so the steady-state approximation applies to the evolution of the hyperfine states populations [22]

$$n_0\,(B_{01}\,I_\nu + C_{01} + P_{01}^{Ly\alpha}) = n_1\,(A_{10} + B_{10}\,I_\nu + C_{10} + P_{10}^{Ly\alpha}) \tag{2.7}$$

Finally, the spin temperature can be expressed as a weighted average of T_γ, T_k and T_α by combining equations (2.1) and (2.7)

$$T_s = \frac{T_* + T_\gamma + y_k T_k + y_\alpha T_\alpha}{1 + y_k + y_\alpha} \tag{2.8}$$

where y_k and y_c are efficiency coefficients

$$y_k = \frac{T_*}{T_k}\frac{C_{10}}{A_{10}} \quad , \quad y_\alpha = \frac{T_*}{T_c}\frac{P_{10}^L}{A_{10}} \tag{2.9}$$

The collisional de-excitation rate is given by the sum of the contributions from collisions with free electrons, protons and other neutral hydrogen atoms: $C_{10} = C_H + C_e + C_p$ with

$$C_H = \kappa\, x_{HI}\, n_H \qquad C_e = \gamma_e\,(1 - x_{HI})\, n_H \qquad C_p = 3.2\,\kappa\,(1 - x_{HI})\, n_H \tag{2.10}$$

Fitting formulas for the effective coefficients κ and γ_e in function of the gas temperature, valid in the range $10 < T_k < 10^4$, are given in [23]

$$\kappa = 3.1 \times 10^{-11}\, {T_k}^{0.357} \exp(-32/T_k)\ \mathrm{cm^3\,s^{-1}} \tag{2.11}$$

$$\log_{10}(\gamma_e/\mathrm{cm^3 s^{-1}}) = -9.607 + 0.5\,\log_{10}(T_k)\,\exp[-(\log_{10} T_k)^{4.5}/1800] \tag{2.12}$$

The Lyα coefficient can be set to zero during the Dark Ages since there are no sources of UV light before the ignition of the first stars. The ionization fraction is close to zero, so C_e and C_p are negligible with respect to C_H.

[1] The 21 cm photons belong to the low-energy tail of the CMB spectrum, where the $h\nu_{21} \ll k_B T_\gamma$ limit holds and the black body spectrum is described by the Rayleigh-Jeans law $I_\nu(T) = \frac{2\,\nu^2 k_B}{c^2}\,T$

2.1.2 21 cm brightness temperature

The spin temperature is not directly observable. What can be measured is the brightness temperature of the neutral hydrogen cloud in contrast with a background radio source, in this case the CMB. This corresponds to the net emission or absorption of 21 cm CMB photons from the neutral hydrogen cloud, described by the equation for radiative transfer along the line of sight [21], which can be written in terms of the brightness temperature T using the Rayleigh-Jeans law

$$\frac{dI_\nu}{d\tau_\nu} = -I_\nu + S_\nu \quad \Longrightarrow \quad \frac{dT}{d\tau_\nu} = -T + T_s \tag{2.13}$$

Here τ_ν is the optical depth of the hydrogen cloud, S_ν is the source function,given by the ratio of the emission and absorption coefficients, and T_s is the excitation temperature of the medium, in this case the spin temperature.

For a cloud of uniform spin temperature, the emerging brightness temperature is

$$T = T_0\ e^{-\tau_\nu} + T_s(1 - e^{-\tau_\nu}) \tag{2.14}$$

with $T_0 = T_\gamma$ since the background source of 21 cm radiation is the CMB. The 21 cm brightness temperature in contrast with the CMB is then given by

$$T_{21} \equiv T - T_\gamma = (T_s - T_\gamma)(1 - e^{-\tau_\nu}) \simeq (T_s - T_\gamma)\ \tau_\nu \tag{2.15}$$

The optically thin medium limit $\tau_\nu \ll 1$ was taken in the last step.

The optical depth of the H cloud is written as in [19]

$$\tau_\nu = \int_0^s \alpha_\nu\ ds = \frac{3c^3 A_{10}}{32\pi\nu_{21}^3}\frac{T_*}{T_s}\frac{x_{HI}\ n_H}{(1+z)\nabla_\parallel u_\parallel} \tag{2.16}$$

where x_{HI} is the fraction of neutral hydrogen and $\nabla_\parallel u_\parallel$ is the comoving gradient of the proper velocity of the gas along the line of sight, including both the Hubble expansion and peculiar velocity contribution. It can also be written as

$$(1+z)\nabla_\parallel u_\parallel = H(z)\left[1 + \frac{(1+z)}{H(z)}\nabla_\parallel v_\parallel^{pec}\right] \tag{2.17}$$

Because of cosmological redshift, we observe the 21 cm line at a frequency $\nu_{obs} = \nu_{21}/(1+z)$ and the observed 21 cm brightness temperature is

$$T_{21}^{obs} = \frac{T_{21}}{1+z} = \frac{T_s - T_\gamma}{1+z}\ \tau_\nu = \frac{3hc^3 A_{10}}{32\pi_B\nu_{21}^2}\frac{x_{HI}\, n_H}{(1+z)\nabla_\parallel u_\parallel}\left(1 - \frac{T_\gamma}{T_s}\right) \tag{2.18}$$

2.2 Evolution of the global signal

The 21 cm temperature is sensitive to the density and thermal state of the medium, so its global evolution, described in [18] and shown in Figure 2.1, can provide information about astrophysical processes taking place at different redshifts. In particular, it has the potential to track the formation of the first stars and galaxies and give some unprecedented insight into the physics of reionization [24].

From (2.8) and (2.18) it is clear how radiative processes tend to drive T_s towards the CMB temperature, bringing the 21 cm signal to zero. Instead collisional processes and the Wouthuysen-Field effect couple T_s with the kinetic temperature of the gas T_k. The 21 cm signal is then observed in absorption ($T_{21} < 0$) if the gas is colder than the CMB and in emission ($T_{21} > 0$) if the opposite is true. Based on these characteristics, it is possible to identify different regimes for the global 21 cm signal, for which a qualitative description is given below.

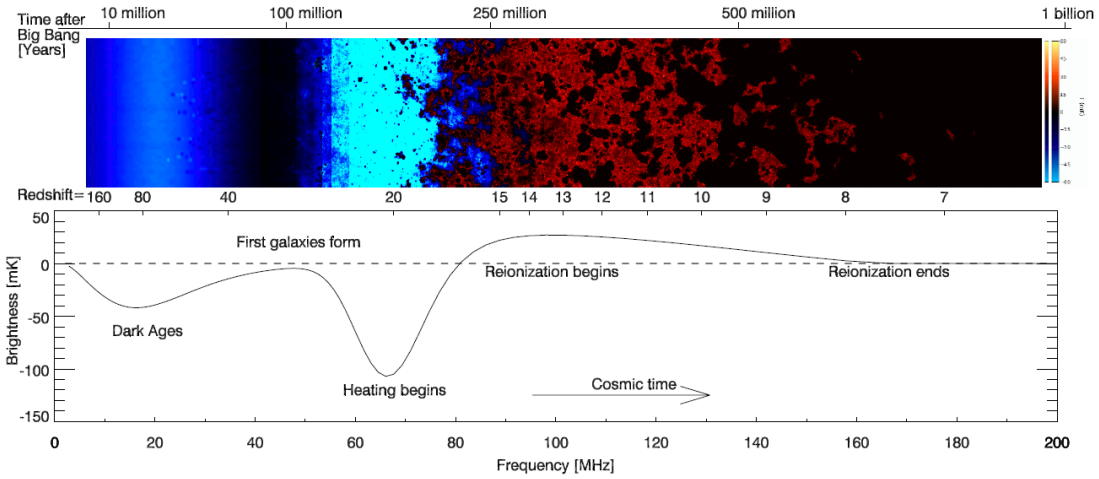

Figure 2.1: Evolution of the average 21 cm global brightness temperature, taken from [18]. Color represents the amplitude of the T_{21} signal in absorption (blue) or emission (red)

- In the early universe the collisional couplings are very effective due to the high gas density and drive the spin temperature towards the kinetic temperature of the gas $T_s \simeq T_k$. After recombination and baryon decoupling, the interactions between the residual free electrons and CMB photons maintain the gas thermally coupled to the CMB ($T_k = T_\gamma$). In this regime we have $T_s \simeq T_k = T_\gamma$ and the 21 cm signal remains close to zero, even if the medium is constituted mainly of neutral hydrogen.
- The 21 cm signal first arises during the cosmic Dark Ages around $z \sim 200$ [25], after baryons thermally decouple from the photons and undergo adiabatic cooling with the expansion. We now have $T_s \simeq T_k < T_\gamma$ and the 21 cm signal is observed in absorption. As the gas density decreases with the expansion, collisional couplings become progressively less effective and the 21 cm signal decreases in amplitude until it goes to zero towards the end of the Dark Ages ($z \sim 30$), when the radiative coupling with the CMB prevails and $T_s \simeq T_\gamma$.
- With the ignition of the first luminous sources (Cosmic Dawn), around $z = 20$, the emitted UV light couples the spin temperature to the cold gas via the Wouthuysen-Field effect. We expect a strong 21 cm signal in absorption, with spacial fluctuations depending on the local Lyα flux.
- As star formation progresses, the X-ray emission from the new light sources heats the IGM above the CMB temperature and the 21 cm signal transitions from absorption to emission, with fluctuations mainly depending on the local gas temperature and ionization fraction. Heating progresses and we reach the regime $T_s \simeq T_k \gg T_\gamma$, where the dependence on T_s in equation (2.20) can be neglected.
- Sometime between $z \simeq 15 - 6$ the light sources ionize the surrounding regions, where the 21 cm signal goes to zero because they don't contain any neutral hydrogen. As the ionization bubbles grow, the global 21 cm signal decreases, until it becomes zero when all the IGM becomes ionized.
- After reionization the 21 cm signal originates only from residual neutral hydrogen clouds that remain in the denser regions of the IGM.

2.3 21 cm fluctuations

Fluctuations in the 21 cm brightness temperature during the Dark Ages trace the underlying cosmic structure with no bias and no dependence on astrophysics. At this time density fluctuations are small and their evolution is still described by linear theory. Thanks to all of these factors, observations of the 21 cm signal from the Dark Ages have the potential to constrain cosmological parameters with high precision.

In this section we derive the expression for the linear fluctuations in the 21 cm brightness temperature from the Dark Ages and their angular power spectrum. From now on T_{21}^{obs} will be referred to as T_{21} for the simplicity of notation. All relativistic effects are neglected in this work. Their contribution is shown to be subdominant in [26], where the 21 cm angular power spectrum is derived from the relativistic Boltzmann equation.

The expression for the observed 21 cm brightness temperature (2.18), expanded at linear order in all possible sources of spacial fluctuations, takes the form [27]

$$T_{21} \simeq \overline{T}_{21}(1+\delta_v) + f_b\,\delta_b + f_T\,\delta_T \tag{2.19}$$

where $\overline{T}_{21}(z)$ is the global 21 cm brightness temperature, defined by setting all perturbations to zero in (2.18) and depending only on the redshift. It is given by

$$\overline{T}_{21} = \frac{3hc^3 A_{10}}{32\pi k_B \nu_{21}^2} \frac{x_{HI}\,\overline{n}_H}{(1+z)H(z)} \left(1 - \frac{T_\gamma}{\overline{T}_s}\right) \tag{2.20}$$

δ_b and δ_T are the relative fluctuations in the baryon density and gas temperature, respectively. During the Dark Ages we can take $\delta_b = \delta_H$, up to negligible corrections. The perturbation in the expansion rate is defined from (2.17) as

$$\delta_v \equiv -\frac{(1+z)}{H(z)} \nabla_\parallel v_\parallel^{pec} \tag{2.21}$$

Fluctuations in the CMB temperature and ionization fraction are negligible, since $\delta_{T_\gamma} \sim 10^{-5}$ and $x_e \sim 10^{-4}$ during the Dark Ages. The expansion coefficients for the different sources of fluctuations are function of the redshift only. Analytic expressions for $f_b(z)$ and $f_T(z)$ can be found in Appendix B of [28].

The evolution of the gas temperature, indicated now with T instead of T_k, can be derived from the first law of thermodynamics as in [17]

$$\dot{T} - \frac{2}{3}\frac{\dot{n}_H}{n_H} T = \frac{2}{3}\dot{q}_c \tag{2.22}$$

Here $\dot{q}_c$ is the Compton heating rate per particle $\dot{q}_c = \frac{3}{2}\Gamma_c(T_\gamma - T)$ and Γ_c is the Compton scattering rate, which is proportional to $x_e\,T_\gamma^4$. The hydrogen number density changes in time because of recombination and photo-ionization and because of the the expansion. The first order perturbed equation for the evolution of temperature fluctuations is then

$$\dot{\delta}_T - \frac{2}{3}\dot{\delta}_b + \Gamma_c \frac{T_\gamma}{\overline{T}}\,\delta_T = 0 \tag{2.23}$$

where fluctuations in x_e and T_γ are being neglected as before.

The solution can be written as

$$\delta_T(\vec{x}, z) = C(z)\,\delta_b(\vec{x}, z) \tag{2.24}$$

with the coefficient $C(z)$ obtained by integrating (2.23) with $\delta_T = 0$ at z = 1000 as initial conditions and assuming $\delta_b \propto a$, which implies the approximation that baryons behave like CDM as soon as they decouple from the photons at the drag epoch.

It is known that baryons fall into the gravitational potential wells created by CDM and give rise to a coherent velocity flow on large scales and advection on small scales. This results in a suppression of the matter power spectrum on small scales and may affect large scales as well, however, these are second order effects and can be neglected in linear theory. The impact of baryon-CDM relative velocity on structure formation is studied in [29].

The coefficient $C(z)$ is plotted in function of redshift in Figure 2.2.

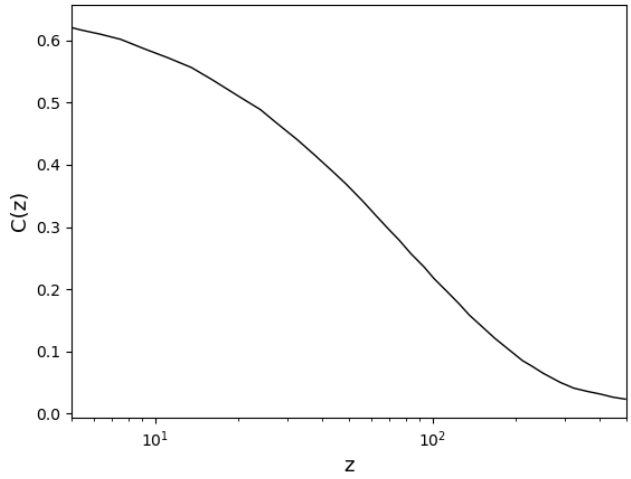

Figure 2.2: Evolution of the linear expansion coefficient $C(z)$. At high redshift $C(z) \to 0$, while at low redshift Compton scattering becomes ineffective and, from equation (2.24) with the last term set to zero, we find $C(z) \to 2/3$.

From equations (2.19) and (2.24), the 21 cm temperature fluctuation $\delta T_{21} \equiv T_{21} - \overline{T}_{21}$ can be written as

$$\delta T_{21}(\vec{x}, z) = \alpha(z)\, \delta_b(\vec{x}, z) + \overline{T}_{21}(z)\, \delta_v(\vec{x}, z) \tag{2.25}$$

The coefficient $\alpha(z) \equiv f_b(z) + C(z)\ f_T(z)$ expresses the variation of T_{21} with respect to the baryon density fluctuation.

The velocity fluctuation (2.21) in Fourier space becomes

$$\delta_v(\vec{k}) = -\frac{i\, k\, v(\vec{k})\, \mu^2}{aH} = f\mu^2 \delta_b(\vec{k}) \tag{2.26}$$

where $\mu = \hat{k}\cdot\hat{n}$ and $\hat{n}$ is the line of sight direction. We used the fact that the velocity field is irrotational in cosmology and substituted equation (1.29) in the second passage.

Expression (2.25) in Fourier space then becomes

$$\delta T_{21}(\vec{k}, z) = \left[\, \alpha(z) + \mu^2\ f(z)\ \overline{T}_{21}(z)\right]\ \ \delta_b(\vec{k}, z) \tag{2.27}$$

The second term in the expression above accounts for redshift space distortions (RDS). We expand on the origin and meaning of this term in section 3.3.1.

From equation (2.27) we can find the angular power spectrum of 21 cm temperature fluctuations at redshift z in function of the matter power spectrum

$$C_\ell^{21}(z) = \frac{2}{\pi} \int dk\, k^2\ \mathcal{T}_\ell(k, z)^2\, P(k, z) \tag{2.28}$$

The transfer function is

$$\mathcal{T}_\ell(k, z) = \int d\chi\ W_z(\chi) \left[\, \alpha(z)\, j_\ell(k\chi) + f(z)\ \overline{T}_{21}(z)\, J_\ell(k\chi)\right] \tag{2.29}$$

The integration is performed along the comoving radial coordinate χ and $W_z(\chi)$ is the window function selecting the frequency band centered in $\nu = \nu_{21}/(1+z)$ and of width $\Delta\nu$, depending on the resolution of the experiment. It is normalized to one $\int_0^\infty d\chi\, W_z(\chi) = 1$. Following the prescription (1.37), the angular dependence in (2.27) traduces into

$$J_\ell \equiv -\frac{\partial^2 j_\ell(k\chi)}{\partial(k\chi)^2} = -\frac{\ell(\ell-1)}{(2\ell-1)(2\ell+1)}\ j_{\ell-2}(k\chi) + \frac{2\ell^2+2\ell-1}{(2\ell-1)(2\ell+3)}\ j_\ell(k\chi) - \frac{(\ell+1)(\ell+2)}{(2\ell+1)(2\ell+3)}\ j_{\ell+2}(k\chi) \tag{2.30}$$

The second order derivative of the Bessel function is expressed in terms of Bessel functions of different order using relation (1.38) as in Appendix G of [30].

Chapter 3

GR tests with the growth history

In order to detect deviations from GR it is necessary to measure the growth history of matter density perturbations together with the expansion. In fact, while some models may be ruled out based on the expansion history alone, there is usually enough freedom to tune different theories to reproduce the desired expansion history, consistent with observational constraints. Changing the theory of gravity, however, affects the growth of perturbations and leaves signatures on the matter power spectrum and on the CMB that are in principle detectable.

Information about the growth history is contained in a variety of observables, among which the growth factor $D(z)$, the ISW effect in the CMB or in the matter power spectrum and the growth rate of matter perturbations $f(z)$. In this work we focus on the growth rate since the ISW is a large scale effect, difficult to constraint because of cosmic variance, and the growth factor presents more degeneracies with other cosmological parameters.

3.1 Linear growth of matter density fluctuations

For a generic modified gravity model, the dynamical equation for the growth of matter density at linear order in the perturbations, in the sub-horizon regime and quasi-static approximation, is [31]

$$\ddot{\delta} + 2H\dot{\delta} = 4\pi G_{eff}\rho_m\delta \tag{3.1}$$

where δ is the gauge-invariant density contrast, which is defined as $\delta = \delta_m + 3aHv/k$ and, in the limit in which we are working, takes the usual expression $\delta = \delta_m = \frac{\delta\rho_m}{\rho_m}$. The effective gravitational coupling G_{eff} depends on the chosen theory of gravity and it is, in general, a function of both time and scale. In the framework of GR it is given by the Newtonian gravitational constant G, as seen in (1.27). Using the definition (1.19), equation (3.1) can be written in the form

$$\ddot{\delta}_m + 2H\dot{\delta}_m - \frac{3}{2}\,\mu(k,z)\; H^2\,\Omega_m\,\delta_m = 0 \tag{3.2}$$

where the parametrization $\mu(k,z) = G_{eff}(k,z)/G$ encodes time and scale-dependent deviations from GR, where $\mu = 1$ and the evolution of δ_m is driven by the expansion and is scale-independent after matter-radiation equality. The same equation is valid for the linear growth factor $D(z)$, following its definition (3.5).

Using definition (1.28) in (3.2) we find the equation for the evolution of the growth rate

$$\frac{d\,f}{d\ln a} + f^2 + \left(\frac{\dot{H}}{H^2} + 2\right) f = \frac{3}{2}\,\mu(k,z)\;\Omega_m\,\delta_m \tag{3.3}$$

During the matter-dominated epoch we can set $\Omega_m = 1$ and $H = 2/3t$ in (3.2). With the ansatz $\delta_m(t) \propto t^\alpha$ we can easily find that the solution for the growing mode scales as $\delta_m \propto a$, which implies

$f = 1$. With the beginning of the accelerated expansion phase, the Hubble friction term in (3.3) increases and the growth is suppressed so we have $f < 1$ and decreasing. Deviations from this behaviour could be a signature of modified gravity.

From equation (3.3) we see how, if GR is the correct description of gravity ($\mu = 1$), the growth rate depends only on time and it is completely determined by the expansion history. In this case (3.3) represents a consistency relation between the two. Instead, if we consider a modified gravity theory with a generic $\mu(t, k)$, the growth history contains some independent information and f could gain scale-dependence and have a different evolution in time. Therefore a discrepancy between the measured growth and its prediction from the expansion history hints at the presence of deviations from GR and allows to distinguish modified gravity models from theories that explain the cosmic acceleration while keeping GR as the valid theory of gravity on all scales.

3.2 The growth index parametrization

Instead of testing predictions of specific modified gravity theories it is more convenient to parameterize the possible deviations from GR in a model-independent way.

For the purpose of detecting deviations from ΛCDM+GR in the growth of perturbations, it is convenient to parameterize the growth as a functional of $\Omega_m(a)$, which completely characterizes the expansion history. The simple and model-independent parametrization

$$f = \Omega_m(a)^\gamma \tag{3.4}$$

reproduces the growth history with good precision for a wide range of models [32].

The parameter γ, referred to as *growth index*, characterizes the growth of density perturbations in the linear regime, apart from the effects of the expansion. Since since $0 < \Omega_m < 1$, a lower value of γ implies faster growth.

The growth factor becomes

$$D(\Omega_m(a)) = \exp\left(\int_1^a \frac{da'}{a'}\Omega_m(a')^\gamma\right) \tag{3.5}$$

If we consider GR to be the correct description of gravity on all scales, equation (3.4) reproduces the growth history found numerically from (3.3) with $G_{eff} = G$ for [33]

$$\gamma = 0.55 + 0.05(1 + w_1) \quad \text{for } w_{DE} \geq -1 \tag{3.6}$$
$$\gamma = 0.55 + 0.02(1 + w_1) \quad \text{for } w_{DE} < -1 \tag{3.7}$$

where w_1 is the DE equation of state parameter at $z = 1$. This solution has accuracy below 0.2% for $0.22 \lesssim \Omega_m \leq 1$, encompassing the entire growth history up to this day.

In ΛCDM, where $w_{DE}(z) = w_\Lambda = -1$, we have $\gamma = 0.55$ and constant. We still expect γ to be about constant and close to this value for dynamical DE models with a time-varying equation of state, provided that GR is the right theory of gravity. In fact γ only has a weak dependence on w_1, which should not deviate a lot from -1 according to observational constraints on $w_{DE}(z)$ [34]. On the contrary, for modified gravity models, the growth index departs significantly from the GR value $\gamma = 0.55$ and acquires time and scale dependence, even when they reproduce the same expansion history as ΛCDM [35]. Such distinct behaviour makes the parameter γ optimal to test GR on large scales.

3.3 Measuring the growth history

3.3.1 Cosmological probes

The linear growth rate is measured mainly through probes of the peculiar velocity field, since $v \propto f$ at linear order on sub-horizon scales. This follows from the fact that the velocity field is irrotational,

so we can write it in terms of a velocity field potential defined by $\vec{v} \equiv -\vec{\nabla}\Phi_v$, where the gradient is in physical coordinates. Using this in (1.29), we find $\nabla^2\Phi_v = Hf\delta_m$, which substituted in the Poisson equation gives

$$\nabla^2\Phi = 4\pi G\,\overline{\rho}_m\delta = \frac{3}{2}\Omega_m H^2\delta_m = \frac{3}{2}\frac{H\Omega_m}{f}\nabla^2\Phi_v$$

If the growth rate f has no scale dependence, this translates into an expression for the peculiar velocity in function of the gravitational potential sourced by the matter field

$$\vec{v} = -\frac{2}{3}\frac{f}{\Omega_m H}\vec{\nabla}\Phi$$

This shows also how, in the linear regime, peculiar velocities are directly proportional to gravitational acceleration $\vec{g} = -\vec{\nabla}\Phi$ so matter moves along the gravitational field lines. Therefore peculiar velocities are sensitive to the gravitational field sourced by the matter distribution and trace matter with no bias. A very small bias could still be present because we measure peculiar velocities of biased tracers, but it's expected to be negligible.

Peculiar velocity surveys

Peculiar velocities can be measured directly for some tracers with peculiar velocity surveys, combining the redshift information with redshift-independent distance measures as shown in [36]. Widely used distance indicators are Cepheid variables, which do not require calibration but are only accessible at small distances (up to $\sim$ 20 Mpc), Type Ia supernovae (SNeIa), the Tully-Fisher (TF) relation for spiral galaxies and the Fundamental Plane (FP) relation for elliptical galaxies. The last three are accessible at larger distance but need to be calibrated.

The downside of direct measures of the peculiar velocity is that the error comes mainly from the precision on the distance measures and increases linearly with it, hence peculiar velocity surveys rapidly lose effectiveness with increasing redshift.

Redshift space distortions

Peculiar velocity statistics are also sensitive to the growth rate of structure. In fact it is possible to obtain information about the statistical properties of the peculiar velocity field through redshift space distortions (RSD) in the 2-point correlation function of some tracer of the matter distribution. This is an observational effect originating from the fact that we deduce distances from redshift assuming that it is caused only by the expansion of the universe while an unknown contribution from the peculiar velocity of the emitters is also present.

On linear scales, the coherent inflow of matter into over-dense regions and the outflows from under-dense regions will produce an additional red or blue-shift on top of the cosmological redshift. Emitters on the far side, with respect to the observer, of a high-density region will have an additional blue-shift and thus appear closer than they really are when the radial position is reconstructed from the redshift, while emitters on the near side will appear farther away. The consequence is an enhancement of clustering along the line of sight, which breaks rotational invariance and introduces anisotropy in the reconstructed matter distribution.

The observed power spectrum for a tracer X is going to be

$$P_X^s(k,\mu) = (\,b_X + f\mu^2\,)^2\,P_X^r(k) \tag{3.8}$$

where $P^r(k)$ is the power spectrum of the real matter distribution and f is the growth rate. This expression was first derived by Kaiser [37] in 1987 and assumes the distant approximation, which restricts its validity to relatively small scales. For larger separations, wide-angle effects become important. A derivation of wide angle corrections is provided in [38].

On smaller non-linear scales, where we have random motion, the resulting effect is a stretching of the matter distribution along the line of sight, often referred to as Fingers of God (FoG), which causes

a suppression of the clustering on small scales. We will not concern ourselves with this effect in this work since we are dealing only with linear scales during the Dark Ages.

3.3.2 Available constraints

It is not possible to measure the growth rate directly with RSD or peculiar velocity surveys, which can only constrain the following parameter combinations:

- the velocity scale parameter $\beta = f/b$, where b is the bias of the chosen tracer.
- the normalized growth rate $f\sigma_8$, where σ_8 is the clustering amplitude at the scale of $8\,h^{-1}$ Mpc. For LIM surveys we have $T_{21}f\sigma_8$, since the power spectrum is proportional to the 21 cm temperature.

Some independent measures or a model for the degenerate parameters are needed in order to obtain constraints on f alone. The most stringent constraints on the growth rate so far were provided by RSD, reaching up to redshift $z \sim 2$.

An up-to date recap of f and $f\sigma_8$ measurements can be found in Table 1 and 2 of [39]. They report 11 direct[1] measurements for f and 20 measurements for $f\sigma_8$, obtained from a variety of cosmological tracers and containing only uncorrelated data. The data points are shown here in Figure 3.1. The reconstruction of the functions $f(z)$ and $f\sigma_8(z)$, performed with Gaussian Processes Regression, is compatible with ΛCDM.

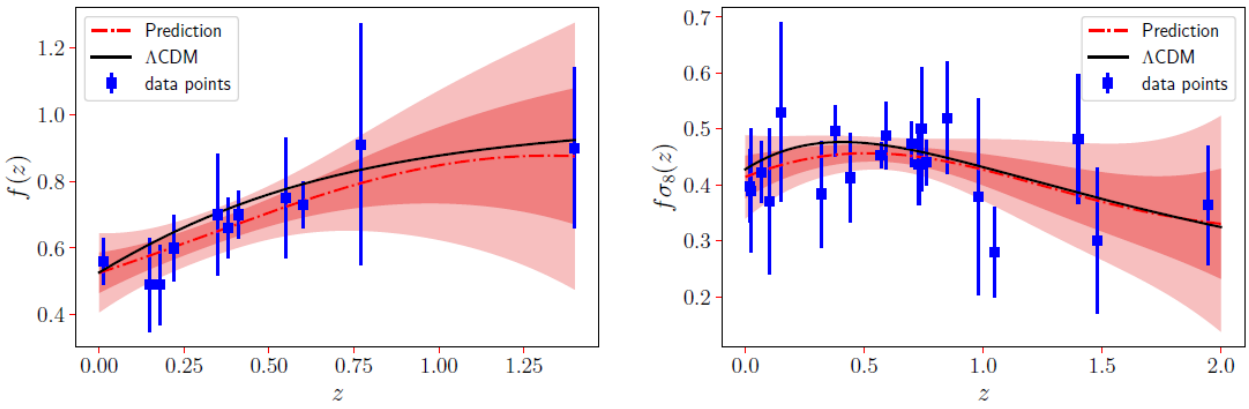

Figure 3.1: Reconstruction of the functions $f(z)$ and $f\sigma_8(z)$ from the data points (red dot-dashed line) compared to the ΛCDM prediction (solid black line). The red areas show the 1σ and 2σ confidence level regions. Taken from [39]

Measurements of the growth factor can be translated in into constrains on the growth index. From (3.4) it follows that the growth index can be found from measures of the growth rate and matter density parameter at the same redshift.

$$\gamma(z) = \frac{\ln f(z)}{\ln \Omega_m(z)} \tag{3.9}$$

An alternative is to express the growth index as a function of the combination $f\sigma_8$ [39]

$$\gamma(z) = \frac{\ln\left(\frac{f\sigma_8(a)}{\int_0^a \frac{da'}{a'} f\sigma_8(a')}\right)}{\ln\left(\frac{af\sigma_8(a)^2}{3\int_0^a da' f\sigma_8(a')\int_0^{a'} \frac{da''}{a''} f\sigma_8(a'')}\right)} \tag{3.10}$$

which is convenient because there is no need to break the degeneracy between f and σ_8 and the expansion history data is not needed. Another advantage is that the dependence on the bias of f

[1] Obtained without the assumption of a cosmological model to eliminate the σ_8 dependence.

and σ_8 cancels out in their combination, making $f\sigma_8$ a bias-independent quantity. A compilation of constraints on γ derived form $f\sigma_8$ is reported in Table 1 of [40].

In [39] the growth index, considered to be a free time-dependent function, is constrained with both methods from the growth data presented above. The result is shown in figure 3.2. In this case the function $\Omega_m(z)$ was reconstructed from the Pantheon SNIa compilation [41]. No statistically significant deviations from the GR behaviour were observed in either case. The only difference between the two is that $f\sigma_8$ data show an excess of growth with respect to ΛCDM+GR ($\gamma < 0.55$) for $z \gtrsim 0.5$, while f data shows the opposite.

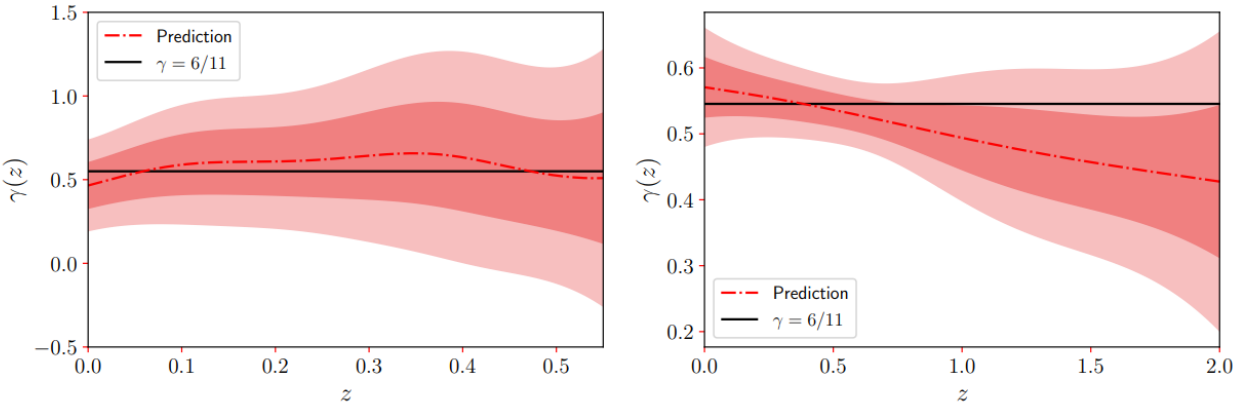

Figure 3.2: Reconstruction of the function $\gamma(z)$ from $f(z)$ and $f\sigma_8(z)$ data (red dot-dashed line), on the left and right panel respectively. The red areas show the 1σ and 2σ confidence intervals and the solid black line marks the GR constant value. Taken from [39].

Chapter 4

Status of 21 cm observations

In this chapter we give an overview of the main achievements of 21 cm intensity mapping so far, focusing on the 21 cm line as a probe of large scale structures, and we discuss what we may expect from future 21 cm observations when it comes to cosmology and fundamental physics. We start by describing the main factors hindering the detection of the 21 cm signal.

4.1 Observational challenges

The 21 cm emission from neutral hydrogen is the only cosmological probe available for the Dark Ages and is also very promising to study Cosmic Dawn and the EoR. However, the detection of the redshifted 21 cm signal becomes increasingly challenging going towards lower frequencies because of the high foreground contamination and the signal from the Dark Ages is completely cut off due to the presence of the atmosphere.

4.1.1 Atmospheric cut-off

Low frequency radio observations from Earth are limited mainly by the presence of the ionosphere, which is completely opaque to frequencies below ~ 10 MHz [42]. Ground-based observations below ~ 30 MHz are still extremely challenging because the ionosphere causes amplitude fluctuations in electromagnetic signals with increasing power towards lower frequencies, at which the signal is also more affected by interference from man-made radio signals.

The 21 cm signal from the Dark Ages is expected in the redshift range $30 < z < 200$, which corresponds to the observed frequency range 7 MHz $\lesssim \nu \lesssim$ 46 MHz. Because of the limitations just described, ground-based 21 cm observations will be restricted to redshifts below $z \sim 30$, so only the very end of the Dark Ages will be visible from Earth.

4.1.2 Foreground contamination

Foreground contamination represents a great challenge when it comes to intensity maps. The foreground is expected to be four to five orders of magnitude larger than the cosmological signal over all frequencies relevant for the redshift 21 cm line [43]. It follows that understanding the properties of the foreground with great precision is of fundamental importance in order to be able to isolate the cosmological information from intensity maps.

When dealing with low frequency radio observations, the foreground is dominated by the galactic synchrotron emission. Other relevant contribution are galactic free-free emission, extragalactic synchrotron emission and terrestrial radio frequency interference (RFI), created by man-made sources and atmospheric events.

The observed synchrotron spectrum at low frequencies follows a decaying power law $T_{sky} \propto \nu^{-\beta}$ [42], where the value of the spectral index β changes with the observed frequency band. Hence, the

foreground increases at lower frequencies, making it more difficult to probe higher redshifts. The power-law spectrum of the synchrotron emission implies that the foreground changes smoothly with frequency, which allows to distinguish it from the cosmological signal and separate it. Foreground removal techniques mainly rely on this characteristic. The effect of foreground residuals on the cosmological information can be further reduced by cross-correlation with galaxy surveys or with other emission lines.

Another issue in intensity mapping is contamination from different lines redshifted to the same frequency band (interloper lines). Fortunately, there is no strong emission from other lines that is redshifted to the frequency range of interest for the 21 cm line, so this effect is minimal for 21 cm observations [44].

4.2 Historical overview

The 21 cm line emission from neutral hydrogen in the interstellar medium was predicted for the first time by H. C. Van de Hulst in 1945 and detected not long after by different research groups in 1951. 21 cm observations were first employed successfully to study the spiral structure of our galaxy and the rotational curve of M13. There were also a number of attempts to detect neutral hydrogen in the nearby IGM through the 21 cm line in absorption or emission against bright extra-galactic radio sources, which failed because the IGM is highly ionized up to at least redshift $z \sim 6$. Howaver, this fact was only later discovered with Lyα observations.

The idea to use 21 cm emission to detect the neutral hydrogen distribution and probe cosmic structure formation at high redshift, when the universe was not ionized, gained attention towards the end of the 90s, following the CMB measurements by the Cosmic Background Explorer (COBE) and the first predictions for the 21 cm signal based on the ΛCDM model.

The first detection of cosmic structure with 21 cm intensity mapping was accomplished in 2008 [45], using the 21 cm data from the HIPASS survey in cross-correlation with an overlapping sample from the 6dFGS galaxy catalogue. They found significant positive correlation up to $3\,h^{-1}$ Mpc of relative distance, with a peak at zero separation due to the galactic HI emission. This study was limited by the fact that the HIPASS survey was designed to detect galaxies and not optimized for intensity mapping. An improvement was obtained in 2010 [46] with a dedicated 21 cm survey from the Green Bank radio telescope (GBT) in the redshift range $0.53 < z < 1.12$ analyzed in cross-correlation with the DEEP2 galaxy survey. They found significant positive correlation out to a relative displacement of $10\,h^{-1}$ Mpc, with amplitude $(157 \pm 42)\ \mu$K at zero separation at redshift $z \sim 0.8$.

The measured correlation of the 21 cm field with galaxies, which are known tracers of the cold dark matter distribution, confirmed the validity of 21 cm intensity mapping as a probe of cosmic structure and sparked the interest that followed in developing the adequate instruments and theoretical framework to improve our understanding of the universe with this new probe.

4.3 Latest results

In this section we go over the achievements of 21 cm intensity mapping observations up to this day.

4.3.1 Detection in cross correlation with galaxy surveys

The 21 cm signal has been detected in cross-correlation with galaxy surveys out to redshift $z = 1.30$ [47], where it's still possible to resolve the emission from single galaxies and have overlap between intensity maps and galaxy catalogues. Above $z \sim 2$ the signal from individual galaxies is too faint to be observed with a sufficient signal-to-noise ratio to make a detection. The advantage of cross-correlating intensity maps with galaxy catalogues is the possibility to better filter out the foreground that plagues LIM observations. This is what has enabled the detection of the 21 cm signal so far.

Measurements of the cross-power spectrum can be used to constrain the parameter combination $\Omega_{HI}\, b_{HI}\, r$, where Ω_{HI} is the neutral hydrogen energy density as a fraction of the present day critical density, b_{HI} is the HI linear bias and r is a phenomenological cross-correlation coefficient that absorbs uncertainties in the modelling. The amplitude of 21 cm temperature fluctuations is proportional to the abundance of neutral hydrogen, which is connected to the matter distribution through $\delta_{HI} = b_{HI}\delta_m$. Therefore, the precision with which these quantities are known determines how well cosmological parameters can be constrained from the detection of the 21 cm power spectrum.

The degeneracy between parameters in the combination constrained by cross-correlations is usually broken by assuming some theoretical model for the b_{HI} and r or by deriving their value from simulations, as in [47, 48], since they are poorly constrained by observations.

Other than with 21 cm intensity maps, the HI density parameter Ω_{HI} has been constrained with galaxy surveys at redshifts lower than $z \simeq 0.25$ and with Damped Lyα Absorption (DLA) measurements at higher redshifts, out to $z \sim 5$. The highest-redshift LIM measurement of Ω_{HI} was recently achieved by the CHIME[1] collaboration at $z = 1.3$ [47], from the CHIME telescope 21 cm intensity maps in cross-correlation with eBOSS galaxy and quasar catalogues. A compilation of Ω_{HI} and b_{HI} constrains obtained with the different techniques just described and updated to 2014 can be found in [49]. Up-to-date plots of the constraints are reported in [48, 47]

4.3.2 Upper limits on the 21 cm power spectrum

The detection of the 21 cm signal in cross-correlation with galaxy surveys is limited by the fact that it only allows to cover volumes dictated by the capabilities of galaxy surveys, when LIM has the potential to reach much higher redshifts and probe larger scales. Hence, the main goal of LIM surveys is to detect the 21 cm signal in auto-correlation. The first generation of low-frequency radio interferometers (LOFAR, GMRT, MWA, PAPER, LWA) didn't achieve this goal but managed to establish upper limits across a wide redshift range, encompassing the Epoch of Reionization and Cosmic Dawn, with improving precision over the years. The second generation of such instruments (SKA, HERA, NenuFAR) is expected to have enough sensitivity to measure the 21 cm power spectrum from the EoR at least.

A compilation of the most recent 95% (2σ) confidence level upper limits on the 21 cm power spectrum from the Epoch of Reionization (EoR) and Cosmic Dawn is reported in figure 4.1. The 2σ upper limit at highest redshift so far, not shown in the plot, was obtained by LOFAR [50] in 2019. They found $\Delta_{21} < 2.12 \times 10^8$ mK^2 at $k \sim 0.038\ h$ Mpc^{-1} in the redshift range $19.8 < z < 25.2$. The redshift evolution of the fiducial 21 cm power spectrum (computed in [51]) is plotted for three different values of k, representative of the range $0.03 < k < 0.4$ Mpc^{-1} over which the upper limits are distributed. The cosmological signal remains over 2 orders of magnitude below the sensitivity of the currently operating low-frequency radio interferometers, but its detection may come in the next few years. The predicted noise curve for SKA [2] lays below the 21 cm power spectrum for most of the EoR and Cosmic Dawn, as shown in the figure 4.1, and the first results from HERA[3] have already set the lowest upper limit on the 21 cm power spectrum from the EoR. The HERA collaboration found $\Delta_{21} < 9.46 \times 10^2$ mK^2 at $k \sim 0.192\ h$ Mpc^{-1} and $z = 7.9$ [52], improving on the previous limits at similar redshifts by over one order of magnitude.

A recent measurement of the global 21 cm temperature at high redshift from EDGES [4] suggests that the amplitude of the 21 cm power spectrum from the EoR and Cosmic Dawn could be larger than expected [54]. They detected an absorption profile in the 21 cm global signal (shown in Figure 4.2) spanning the redshift range $20 \lesssim z \lesssim 15$ and centered in $z \sim 17$ with an amplitude of $\overline{T}_{21} \sim 0.53$ K, which is more than twice what is predicted by the ΛCDM model. In fact, even though astrophysics is not well constrained at these redshift due to the lack of direct observations, this detection is difficult

[1] http://chime-experiment.ca/
[2] https://www.skatelescope.org
[3] https://reionization.org/
[4] Experiment to Detect the Global Epoch of Reionization Signature

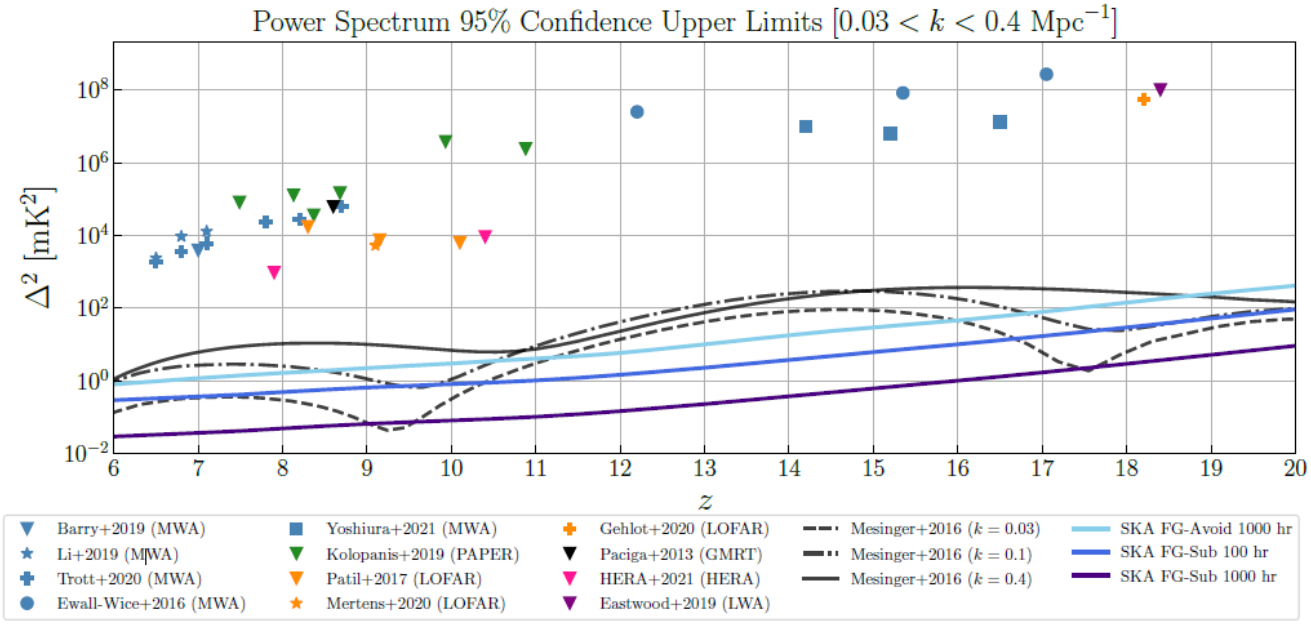

Figure 4.1: 95% upper limits on the 21 cm power spectrum over the redshift range $6 < z < 20$, compared with the predictions for the 21 cm power for $k = 0.03, 0.1, 0.4\text{Mpc}^{-1}$ (in black) and 95% SKA sensitivity curves for different foreground removal techniques (in blue). Taken from [53].

to explain with astrophysical effects alone. In [55] the 21 cm temperature evolution with redshift is studied for 193 different astrophysical models, varying the optical depth, star formation and X-ray heating parameters. The largest amplitude of the absorption signal remains below 0.25 K, as seen in Figure 4.3.

Some non standard scenarios were proposed to explain the extra cooling of the IGM implied by the EDGES detection, including early dark energy and interaction between baryons and dark matter. Finally, it is still to be considered that this detection has yet to be confirmed by independent experiments.

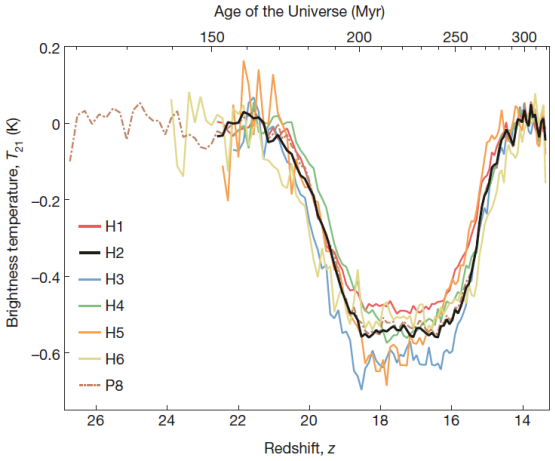

Figure 4.2: Best fit for the absorption profile measured with different hardware configurations. The solid black line corresponds to the setup with the highest signal-to-noise ratio. Taken from [54]

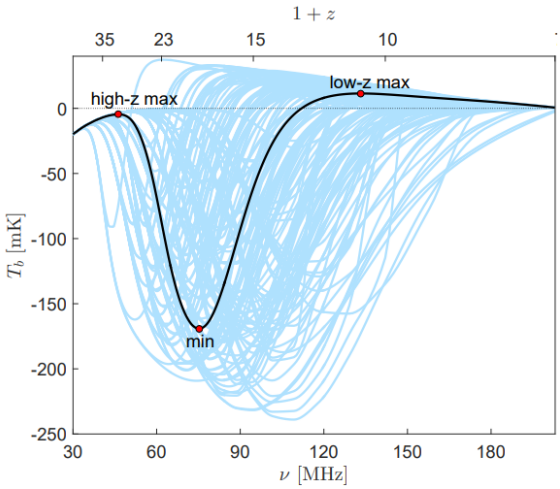

Figure 4.3: 21 cm temperature as a function of redshift for 193 different astrophysical model. Taken from [55].

4.4 Future prospects

Intensity mapping is a relatively new observational technique, with not many datasets available and a lot of room for improvement in instrumental sensitivity and data analysis methods. IM has a lot more potential compared to its present-day status and recent years have seen a great effort to fully explore it, with the development of more advanced instruments, optimization of foreground-removal techniques and improved theoretical models of the LIM signal from different epochs.

The new generation of ground-based LIM experiments will become operational in the next few years and, thanks to improvements in resolution and sensitivity, will allow for the detection of the 21 cm signal over a wide range of scales and redshifts, potentially reaching the end of the Dark Ages at $z \sim 30$. They will achieve cosmological constraints competitive with the CMB and future large galaxy surveys (Euclid, LSST, DESI) or surpassing them in precision in some cases.

In this section we provide an overview of the constrains on cosmology and fundamental physics that may come with future LIM surveys.

Expansion history

LIM has great potential to constrain the expansion history on a wide range of redshifts through measurements of the BAO feature in the matter power spectrum. Available constraints on the expansion reach $z \sim 2.4$ because of the current limitations of measurements with standard candles, galaxy surveys and the Lyα forest. Most data points are still below $z \sim 1$ and their error is dominated by spacial variance. IM offers the possibility to map larger volumes, thus improving the precision on the current BAO measurements and extending their redshift range. Future galaxy surveys, like DESI and Euclid, will also probe larger scales but they will be limited to redshifts $z \lesssim 2$. The next generation of LIM experiments is expected to measure the BAO scale out to $z \sim 9$, with precision below $2-3\%$ in the redshift range $3 < z < 7$ [56]. The LIM survey with SKA will be able to constrain the Hubble rate $H(z)$ in the redshift range $2 \lesssim z \lesssim 6$ with sub-percent level precision [57].

This is particularly relevant because of the tension between direct measurements of the the Hubble parameter at low redshifts and its value inferred from the CMB , which has surpassed 4σ with recent measurements [58]. Obtaining precise measurements of the BAO scale beyond $z \sim 2$ is also important to constrain dynamical dark energy, since this is where most models exhibit deviations from a cosmological constant behaviour $w = -1$, as shown in [59].

Growth history

As shown in the previous chapter, the growth rate has been constrained with with $5-30\%$ precision up to redshift $z \sim 2$ and constraints in the range $1 \lesssim z \lesssim 2$ don't go below the 20% level. Future LIM surveys with SKA will bring an improvement of one order of magnitude for growth rate constraints below $z \sim 2$, reaching the $0.5-3\%$ precision level. Even though these constraints are not competitive with future galaxy surveys, that are expected to reach $\sim 0.4\%$ precision over this redshift range, they will still provide an independent measure of the growth. The unique contribution from LIM surveys will be to extend the redshift range for $f\sigma_8$ measurements. SKA-Low will achieve $\sim 10\%$ constraints on $f\sigma_8$ over the redshift range $2 < z < 6$, which is beyond the capabilities of any other survey.

Exotic energy injection

The 21 cm signal during the Dark Ages is sensitive to the thermal state of the IGM, which makes it a good probe for exotic energy injection and therefore can be used to constrain models of decaying and annihilating dark matter and DM-baryons interactions, as explored in [60] and [61].

Large scale effects

IM surveys will give access to extremely large volumes, beyond the reach of other observational techniques, thus offering a unique opportunity to measure ultra-large scales effects. Among these,

primordial non-gaussianity and GR corrections to the matter transfer function, which can be used to constrain inflationary models and test gravity on large scales. On such large scales, a multi-tracer analysis is needed to reduce cosmic variance and enable the detection of these effects. SKA intensity maps in combination with overlapping Euclid or LSST surveys are expected to constrain f_{NL} with an error $\sigma(f_{NL}) < 1$ [43], improving on the current best bound from Planck $f_{NL} = 0.8 \pm 5.0$ and allowing to differentiate between single field and multi-field models of inflation. SKA is also expected to detect relativistic corrections for the first time.

ISW effect

The ISW effect, arising from the variation in time of the effective gravitational potential $\Phi_{eff} = (\Phi + \Psi)/2$, has already been detected from the CMB alone and in cross correlation with galaxy number counts. The presence of an ISW contribution from the matter-dominated epoch is a distinctive signature of modified gravity. In fact, according to ΛCDM+GR, Φ_{eff} is constant during during the matter era and the ISW effect arises only at late times when the cosmological constant starts to dominate and the potential decays with cosmic acceleration. In modified gravity models, instead, the potential could start to evolve already during the matter era.

The 21 cm photons from high redshifts are affected by the evolution of the effective potential similarly to the CMB, hence the ISW effect could also be measured from the cross-correlation of the high-redshift 21 cm signal with galaxy surveys, as described in [62]. Another possibility to measure the ISW effect is through cross-correlation between the CMB and 21 cm intensity maps from low redshift, used to trace LSS instead of galaxy catalogues.

EoR physics

Multi-line intensity mapping is a powerful probe of the epoch of reionization, which is currently poorly constrained. The 21 cm signal sourced by neutral regions of the IGM can be used in combination with other lines emitted from ionized regions (like CO, CII, Lyα) to trace the evolution of reionization bubbles and gain statistical information on their size and on the ionization fraction in function of redshift [13]. The cross-correlation between the two will allow for a better understanding of the physics of reionization and of its sources. The expected anti-correlation of the 21 cm emission with ionized regions will also be useful to confirm whether the measured 21 cm signal from the EoR has cosmological origin.

Photometric redshift calibration

Thanks to their high redshift resolution, intensity maps can be used to calibrate the redshift distribution of other tracers of large scale structure characterized by high redshift uncertainties, like photometric surveys and radio continuum surveys, and consequently improve their capability to constrain cosmological parameters, as detailed in [63]. This can be done with the clustering based redshift (CBR) method, which is based on the fact that overlapping surveys trace the same underlying structure and are expected to be spacially correlated. The amplitude of the angular cross-correlation between the sample of unknown redshift and consecutive narrow redshift bins of the high redshift resolution sample depends on the redshift distribution of the former and can be used to infer it.

It was shown in [64] that, with a similar calibration using spectroscopic surveys, it's possible to achieve a substantial improvement in cosmological constraints from photometric and radio continuum surveys. Despite allowing for very precise redshift measurements, spectroscopic surveys are quite time consuming and expensive and lose effectiveness for $z \gtrsim 2$. The use of intensity maps for CBR calibration would extend the redshift range over which this technique is applicable, provided that the current difficulties with foreground contamination will have been overcome.

4.5 Space-based observations

The next generation of ground-based low-frequency radio interferometers will bring substantial improvements in sensitivity and is predicted to achieve the detection of the 21 cm signal from the EoR and Cosmic Dawn. However, issues connected to the presence of the ionosphere and to RFI will be impossible to circumvent with observations from Earth, leaving the most of the Dark Ages beyond the capability of ground-based instruments.

Observations from space have the great advantage of eliminating both problems and would give access to radio frequencies down to 100 kHz, allowing to observe the 21 cm emission from the entire duration of the Dark Ages. Space is also a very stable environment in comparison to the Earth's surface, not subjected to rapid temperature variations and atmospheric phenomena, which allows for better instrument calibration. Galactic and extra-galactic foreground remains a problem and extremely accurate foreground modeling and removal techniques will be needed in order to isolate the cosmological signal, especially at the lower frequencies observable from space where the synchrotron emission further increases in power.

Possible locations for space-based instruments are the far-side of the Moon, the lunar orbit and the second Sun-Earth Lagrangian point (L2), where they would be shielded from the interference from both the Sun and the Earth. There are currently various proposals for space-based instruments to observe the 21 cm fluctuations and global signal from the Dark Ages, for which a list and brief description is given in [65].

A study for a mission to place a low-frequency interferometer (FARSIDE) on the far side of the Moon, founded by NASA, was completed in 2019[5]. The concept is very promising and still under development [66]. A proposal on how to deploy the array with technology already existing or currently under development was recently advanced in [67].

[5]Final report available at https://sservi.nasa.gov/articles/farside-final-report/

Chapter 5

Methodology and results

In this chapter we present our results, after introducing the main tools and methods used to obtain them.

5.1 Tomography

The tomographic approach consists in studying the angular correlation of the chosen tracer on spherical shells obtained by dividing the observed volume in bins along the radial direction. Tomography has some advantages over the use of the 3D power spectrum when the aim is to estimate cosmological parameters [68, 69]. In fact, in order to reconstruct the 3D power spectrum we need to assume a fiducial cosmological model to transform redshifts into radial distances. This passage is not needed for tomographic analysis, which can be carried out in a model-independent way. For the 3D analysis, if the assumed cosmology differs from the true one, radial and transverse distances are scaled differently, which introduces anisotropy in the power spectrum. This is known as the Alcock–Paczynski (AP) effect [70] and is partially degenerate with the anisotropy introduced by RSD. The AP effect can be used to constrain the expansion history, however it could represent a problem in our case, given that we focus on the growth of matter fluctuations.

With a tomographic approach the evolution of the background quantities with redshift is naturally accounted for, while it's neglected within the same wide redshift bin when working in 3D. This is particularly relevant for HI intensity mapping because of the wide redshift range that it can potentially probe. Finally, the tomographic formalism is suitable to perform cross-correlations between different redshift bins and with other LSS tracers. Differently from 3D statistics, some of the radial information is lost when projecting into tomographic redshift bins but this can be limited by a good binning strategy.
In this case it is convenient to choose bins not too large with respect to the resolution of the survey, which needs to be high not to lose radial information. Redshift-dependent functions are also assumed to be constant in the same bin.

5.2 Forecast

We use Bayesian statistics and the Fisher information matrix to determine the precision with which future surveys will be able to measure parameters of interest, before conducting the experiment.

Our universe is one of the possible realizations of an underlying theory, which is described by a set of parameters θ_α, with $\alpha = 1, 2, ...n$. The probability that an observed data set corresponds to one of the realizations of a given theory is expressed by the likelihood function $\mathcal{L}(\vec{\theta})$. The Fisher information matrix is defined as [71]

$$\mathcal{F}_{\alpha\beta} = -\left\langle \frac{\partial^2 \ln \mathcal{L}(\vec{\theta})}{\partial\theta_\alpha \partial\theta_\beta} \right\rangle \tag{5.1}$$

and, under the assumption that the likelihood surface is well approximated by a multi-variate Gaussian close to its maximum, it contains information about the errors and covariance of the theory's parameters. This is true in most cases of interest, thanks to the central limit theorem. The angle brackets indicate the ensemble average over different realizations of the underlying model. This is performed over the observational data following the fair sample hypothesis, according to which we can consider well separated patches of the universe as independent realizations. The derivatives are evaluated at the fiducial value of the model parameters.

When working with the angular power spectrum and under the assumption that the data is Gaussian-distributed, the Fisher matrix can be written as

$$\mathcal{F}_{\alpha\beta} = \sum_{z,\ell} \frac{\partial C_\ell}{\partial \theta_\alpha} \frac{\partial C_\ell}{\partial \theta_\beta} \frac{1}{\sigma^2_{C_\ell}} \tag{5.2}$$

where with C_ℓ we indicate the observed angular power spectrum, given by the sum of signal and instrumental noise, and σ_{C_ℓ} is its error. This is valid under the assumption that different multipoles are uncorrelated so that the covariance matrix is diagonal, which is the case on linear scales and for full sky coverage ($f_{\rm sky} = 1$) [72]. In realistic surveys, partial sky coverage introduces correlations between different modes, which we neglect in this work. According to the laws of probability, when dealing with independent data sets, the total likelihood is the product of their individual likelihoods, so the Fisher matrix becomes their sum. Therefore, when considering independent redshift bins, we can sum over the Fisher matrix at each redshift for the tomographic analysis.

The covariance matrix is $C = \mathcal{F}^{-1}$, therefore the error on the parameter θ_α is given by the corresponding diagonal component of the inverted Fisher matrix

$$\sigma_{\theta_\alpha} \geq \sqrt{(\mathcal{F}^{-1})_{\alpha\alpha}} \tag{5.3}$$

The diagonal elements contain the information about correlation between different parameters. With the Fisher analysis, the uncertainties and correlations with all the other parameters that are measured at the same time are also taken into account in the estimate of the marginalized error on a single parameter. The errors will be smaller if the elements of the Fisher matrix are larger, which corresponds to a higher sensitivity of the data, in this case the C_ℓs, to the variation of the parameters and to a smaller error on the measured data. The constraining power of the survey increases if the observable is measured with greater precision and it is more sensitive to the variation of the parameters of the model.

Because of the various approximations taken, the Fisher forecast is indicative and it serves as a lower limit on the precision that could be reached by the real experiment. The measured error will be larger or, at best, equal to the one predicted with the Fisher analysis. This technique still offers the great advantage of being a lot faster and cheaper than all of the alternatives, like numerical simulations, and therefore plays an important role in experimental design.

5.3 Experimental setup

The angular power spectrum of the instrumental noise for a radio interferometer with uniformly distributed antennas at the observed frequency ν is [73]

$$C_\ell^N = \frac{(2\pi)^3}{\Delta\nu\, t_{\rm obs}} \left(\frac{T_{\rm sys}(\nu)}{f_{\rm cover}\ \ell_{\rm cover}(\nu)} \right)^2 \tag{5.4}$$

where $\Delta\nu$ is the bandwidth, $t_{\rm obs}$ is the observation time and $f_{\rm cover}$ is the fraction of the interferometer's area covered with antennas. For a non-uniform distribution of the antennas, which is the case for realistic arrays, the coverage in Fourier space can change with ℓ so the parameter $f_{\rm cover}$ needs to be substituted by a function $f(\ell)$ describing the geometry of the array along with the coverage. For the scope of this work it's enough to consider the idealized case of uniformly distributed antennas.

ℓ_{cover} is the maximum observable multipole, given by

$$\ell_{\text{cover}} \equiv \frac{2\pi D_{\text{base}}}{\lambda_{\text{obs}}} = \frac{2\pi D_{\text{base}}}{\lambda_{21}(1+z)} \tag{5.5}$$

where λ_{obs} is the wavelength of the observed radiation and D_{base} is the largest baseline of the interferometer, roughly given approximately by its size. ℓ_{cover} corresponds to the smallest observable scale so it gives a measure of the resolution of the interferometer, which decreases with the redshift and increases with D_{base}.

At low radio frequencies, the main contribution to the system temperature is given by the sky temperature, which is dominated by galactic synchrotron radiation so we can take the approximation [19]

$$T_{\text{sys}}(\nu) \approx T_{\text{sky}} = 180 \left(\frac{\nu}{180\,\text{MHz}}\right)^{\beta} \text{K} \tag{5.6}$$

In this work we use $\beta = -2.62$, derived from measurements of the sky brightness temperature in function of frequency made by EDGES [74].

The uncertainty on the observed 21 cm angular power spectrum at a given multipole ℓ is

$$\sigma_{C_\ell} = \sqrt{\frac{2(C_\ell^{21} + C_\ell^N)^2}{(2\ell+1) f_{\text{sky}}}} \tag{5.7}$$

where f_{sky} is the fraction of sky covered by the survey and C_ℓ^{21} is the signal, modeled in section 2.3. This expression accounts for detector noise and cosmic variance.

5.4 Methods and settings

5.4.1 Survey parameters

We consider 5 different experimental configurations for forthcoming surveys: two for the ground-based radio interferometer Square Kilometer Array (SKA) and three for a futuristic telescope on the far side of the moon, the Lunar Radio Array (LRA). The first SKA configuration is for the instrument currently under construction and expected to become operational around 2030, while the second one is for an advanced version that represents the limit to what can be achieved with 21 cm observations from earth.

In each case we consider all sky surveys ($f_{\text{sky}} = 0.75 \sim 30000\,\text{deg}^2$) with a bandwidth of $\Delta\nu = 1\,\text{MHz}$. The specifics of each survey are reported in Table 5.1.

Experiment	D_{base}[km]	f_{cover}	t_{obs}[yr]	$\ell_{\text{cover}}(z=30)$
SKA	6	0.02	5	5791
aSKA	100	0.2	10	96516
LRA1	30	0.1	5	28955
LRA2	100	0.5	5	96516
LRA3	300	0.75	5	289548

Table 5.1: Instrument specifications for different configurations of SKA and LRA

5.4.2 Binning strategy

We study the angular power spectrum on a single redshift slice at $z = 30$ for all experimental configurations. In the case of LRA we also perform a tomographic study with 40 independent redshift bins of width $\Delta\nu = 1$, set by the bandwidth, in the range $30 < z < 200$, given that from the Moon it's possible to observe the 21 cm signal redshifted to these frequencies. In [27] it is shown that neglecting the

correlation between redshift bins defined in this way is a safe assumption. They define the correlation length as the radial separation between redshift slices at which the cross-correlation angular power spectrum becomes less than 1/2 the auto correlation C_ℓs and find that it corresponds to a frequency interval lower than 0.5 MHz for all ℓs.

5.4.3 Fiducial model

We consider the following set of free parameters for the Fisher analysis

$$P = [\ \theta_s,\ \omega_{\rm cdm},\ \omega_b,\ \ln(10^{10}A_s),\ n_s,\ \gamma\ ]$$

The fiducial values for the ΛCDM parameters, reported in Table 5.2, are taken from the Planck 2018 TT,TE,EE + low-E results [1]. We adopt the GR value for the growth index $\gamma = 0.55$ as fiducial, as discussed in section 3.2.

parameter	fiducial value	description
$100\theta_s$	1.04109	θ_s is the angular size of the sound horizon
$\omega_{\rm cdm}$	0.1202	cold dark matter abundance ($\omega_{\rm cdm} = \Omega_{\rm cdm}h^2$)
ω_b	0.02236	baryonic matter abundance ($\omega_b = \Omega_b h^2$)
$\ln(10^{10}A_s)$	3.045	A_s is the amplitude of the primordial power spectrum
n_s	0.9649	spectral index of the primordial power spectrum

Table 5.2: ΛCDM fiducial parameters

We use a prior on A_s from the TT,TE,EE + low-E Planck 2018 results [1] because of the high degeneracy with γ. This is due to the fact that a change in the growth index mainly affects the matter power spectrum from the Dark Ages through a variation of the growth factor $D(z)$, which determines its amplitude together with A_s.

5.4.4 C_ℓ^{21} computation

We compute the angular power spectrum of the 21 cm fluctuations with an internal code that takes the transfer function for the matter power spectrum at $z = 0$ in input from `CLASS` [5], along with a few other quantities needed to find the global 21 cm brightness temperature, like the kinetic temperature and the ionization fraction. The coefficients $f_b(z)$ and $f_T(z)$, needed to compute the factor $\alpha(z)$, are found numerically as the derivative of $\overline{T}_{21}(z)$ with respect to $n_H(z)$ and $T_k(z)$, in that order.

In order to save computational time, we use the flat sky approximation for $\ell \geq 1000$ as described in as in [27]. In this approximation (2.28) and (2.29) simplify to

$$C_\ell^{21}(z) = \frac{2}{\chi^2}\int_0^\infty \frac{dk_\parallel}{(2\pi)^2}\,|\widetilde{W}(k_\parallel)|^2\left[\alpha(z) + \left(\frac{k_\parallel}{k}\right)^2 f(z)\,\overline{T}_{21}(z)\right]^2 P\left(k_\parallel, \frac{\ell}{\chi}\right) \tag{5.8}$$

where χ is the comoving distance corresponding to the redshift bin center, $k_\parallel$ is the wave-vector component along the line of sight and the orthogonal component is $k_\perp = \ell/\chi$. $\widetilde{W}(k_\parallel)$ is the Fourier transform of the window function.

5.5 Results

The amplitude of the 21 cm temperature angular power spectrum during the Dark Ages reaches a maximum around $z = 50$ and decreases again going towards $z = 30$ because of the decrease in absolute value of $\overline{T}_{21}$. This is shown in Figure 5.1, where we plot the fiducial C_ℓ^{21} at different redshifts in the range $30 < z < 200$.

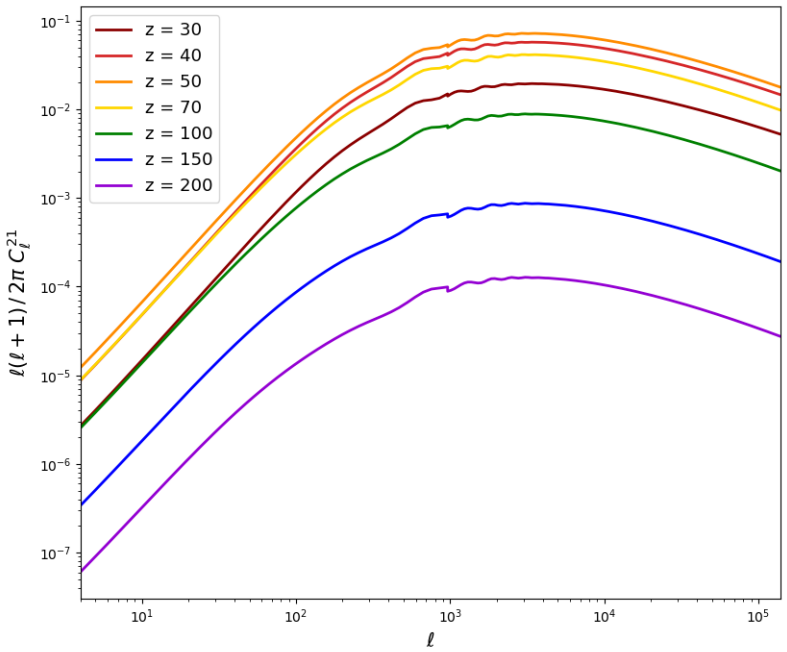

Figure 5.1: Angular power spectrum of 21 cm temperature fluctuations at different redshifts during the Dark Ages.

In Figure 5.2 we shown the evolution with redshift of the signal-to-noise ratio, calculated as $S/N = \sqrt{\sum_\ell \left(C_\ell^{21}/C_\ell^N\right)^2}$ for each redshift bin. Even tough the amplitude of C_ℓ^{21} peaks at $z \sim 50$, the signal-to-noise ratio during the Dark Ages is maximum at $z = 30$ and decreases with redshift for all LRA configurations. This behaviour follows from the fact that that C_ℓ^N increases with redshift more rapidly than C_ℓ^{21} in the range $30 < z < 50$.

According to the S/N plot we expect SKA to have no constraining power over the Dark Ages. aSKA is expected to perform better than LRA1 and to be comparable with LRA2 for observations at $z = 30$ only. LRA3 should provide the best constraints among all instruments taken in exam in this work. The above considerations are confirmed by the analysis that follows.

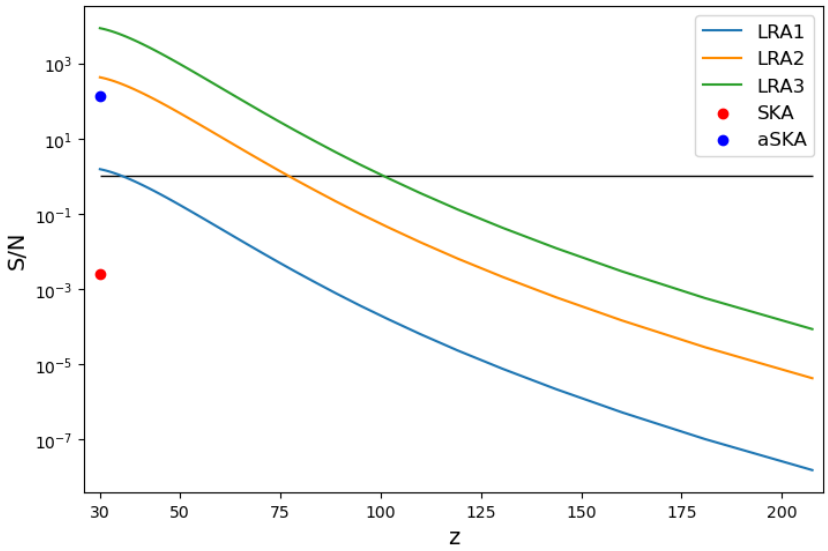

Figure 5.2: Evolution with redshift of the signal-to-noise ratio (S/N) for the different configurations of SKA and LRA. The solid black line marks S/N= 1.

We forecast the marginalized constraints on the growth index γ and on the growth rate $f(z)$ from the angular power spectrum of 21 cm temperature fluctuations observed at $z = 30$, for each experimental configuration described in Table 5.1. In the case of LRA we also derive constraints on γ performing a tomographic analysis over the redshift range $30 < z < 200$ and constraints on $f(z)$ for each redshift bin, modeling it as a redshift-dependent step function. The results are reported in Table 5.3.

Experiment	z	σ_γ/γ	σ_f/f
SKA	$z = 30$	3.98×10^3	6.17×10^2
aSKA	$z = 30$	1.68×10^{-1}	4.60×10^{-2}
LRA1	$z = 30$	6.52	1.04
	$30 < z < 200$	1.39	-
LRA2	$z = 30$	1.03×10^{-1}	3.40×10^{-2}
	$30 < z < 200$	4.42×10^{-2}	-
LRA3	$z = 30$	6.16×10^{-2}	2.22×10^{-2}
	$30 < z < 200$	3.10×10^{-2}	-

Table 5.3: Marginalized 68% C.L. relative errors on the growth index and growth rate, forecasted for each configuration of SKA and LRA.

According to our forecast, SKA will not be able to constrain the growth of structure during the Dark Ages. This is consistent with the fact that the signal-to-noise on the 21 cm angular power spectrum measured by SKA is well below unity at $z = 30$. Instead, a more sensitive instrument like aSKA could achieve constraints on the growth index competitive with the best low-redshift measurements available today ($\sim 10\%$ accuracy). Because of its large baseline aSKA performs better than LRA1, even when using tomography, and achieves similar precision as observations at $z = 30$ with LRA2, which only improves on the aSKA constraints by a factor ~ 1.6. Constraints on the growth rate at $z = 30$ have a similar behaviour.

It will be possible to constraint γ below the 5% precision level only with tomographic analysis, which brings an improvement with respect to the aSKA relative errors of a factor ~ 3.8 for LRA2 and ~ 5.4 for LRA3. Observations at $z = 30$ won't achieve this goal, even if performed with a much more sensitive instrument like LRA3.

The forecasted constraints for the growth rate at $z = 30$ have higher accuracy than those on γ for all instruments and achieve a precision level below 5% for aSKA, LRA2 and LRA3. In Figure 5.3 we compare the evolution with redshift of the constraints obtained on $f(z)$ for the three configurations of LRA taken in exam. From the plot it's evident how LRA1 won't be able to constrain the evolution of the growth rate during the Dark Ages. An instrument like LRA2 can achieve constraints of the growth rate below 10% precision over the redshift range $30 < z \lesssim 55$. LRA3 extends this range to $z \sim 80$, with improvement of a factor ~ 1.6 on the forecasted errors. Above the aforementioned redshifts the error on the growth rate increases rapidly, spanning a few orders of magnitude before we reach $z = 200$ and leaving $f(z)$ unconstrained for $z \gtrsim 100$, even for observations from the surface Moon with an advanced instrument like LRA3.

For the three configurations of LRA we forecast 68% C.L. marginalized constraints on $f(z)$ considering larger redshift intervals around the center values reported in Table 5.4. We stop at $z = 80$, when this type of analysis is no longer possible because the redshift bins become too large to have enough to combine over the chosen intervals. The error bars on $f(z)$ for each interval are shown in Figure 5.4 for LRA2 and LRA3.

The combination of multiple redshift bins allows to improve on the constraints on $f(z)$, especially at

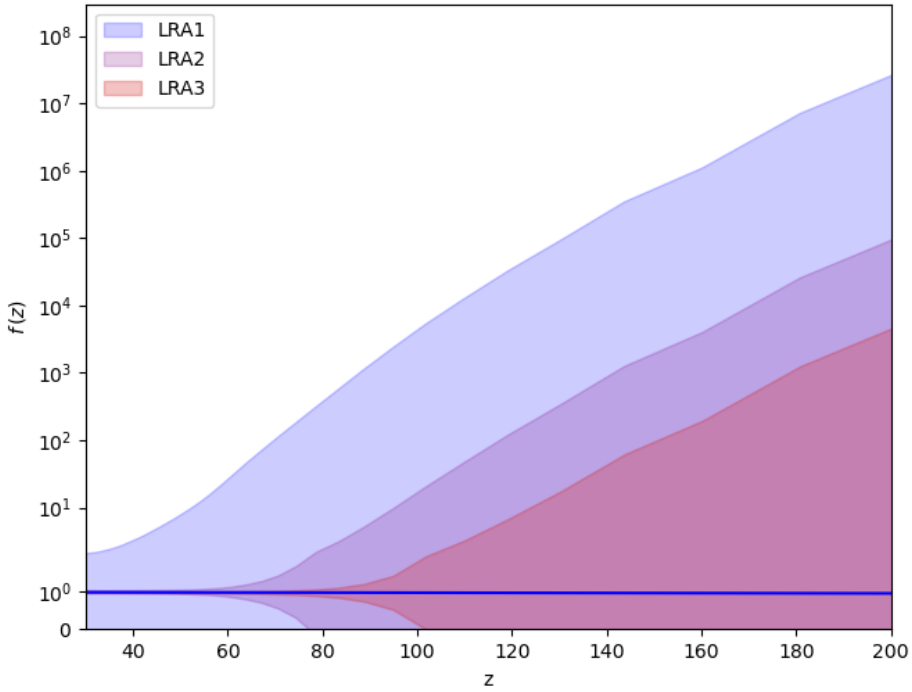

Figure 5.3: 68% confidence level constraints on $f(z)$ for each redshift bin over the redshift range $30 < z < 200$, for different configurations of LRA. The blue line marks the value of $f(z)$.

lower redshifts where the bin centers are more closely spaced. LRA3 will achieve sub-percent precision level on growth rate measures for the two lower redshift intervals, centered at $z = 32.5, 40$. In the case of LRA2 we find constraints below 10% out to $z = 60$, extending the range over which $f(z)$ is constrained with respect to the single redshift bin analysis. We also see an improvement on growth rate constraints from LRA1, however they are still not competitive with those from a ground-based instrument like aSKA.

z	LRA1	LRA2	LRA3
32.5	4.38×10^{-1}	1.31×10^{-2}	8.27×10^{-3}
40	6.74×10^{-1}	1.29×10^{-2}	7.27×10^{-3}
50	2.84	2.46×10^{-2}	1.03×10^{-2}
60	10.74×10^{-1}	5.70×10^{-2}	1.41×10^{-2}
70	56.65×10^{-1}	2.30×10^{-1}	2.69×10^{-2}
80	2.79×10^{2}	1.03	7.42×10^{-2}

Table 5.4: Marginalized 68% C.L. relative errors on the growth rate forecasted at different redshifts for each configuration of LRA.

In Figure 5.5 we show the 68% confidence regions around the fiducial parameters forecasted for LRA2. We compare observations at a single redshift bin at $z = 30$ with the tomographic analysis over the redshift range $30 < z < 200$. The confidence regions obtained for the other configurations of LRA, not shown here, have similar characteristics. We found that the correlation between parameters doesn't change appreciably when considering observations from different instruments at $z = 30$. This is true for all parameter combinations, except $\ln(10^{10}A_s) - \gamma$, for which the negative correlation increases as the error on γ decreases. We interpret this as the effect of setting a prior on $\ln(10^{10}A_s)$. The degeneracy between parameters is reduced when using tomography. This effect is most evident for the parameters γ and ω_b, which have high anti-correlation for observations at $z = 30$ with all instruments. The

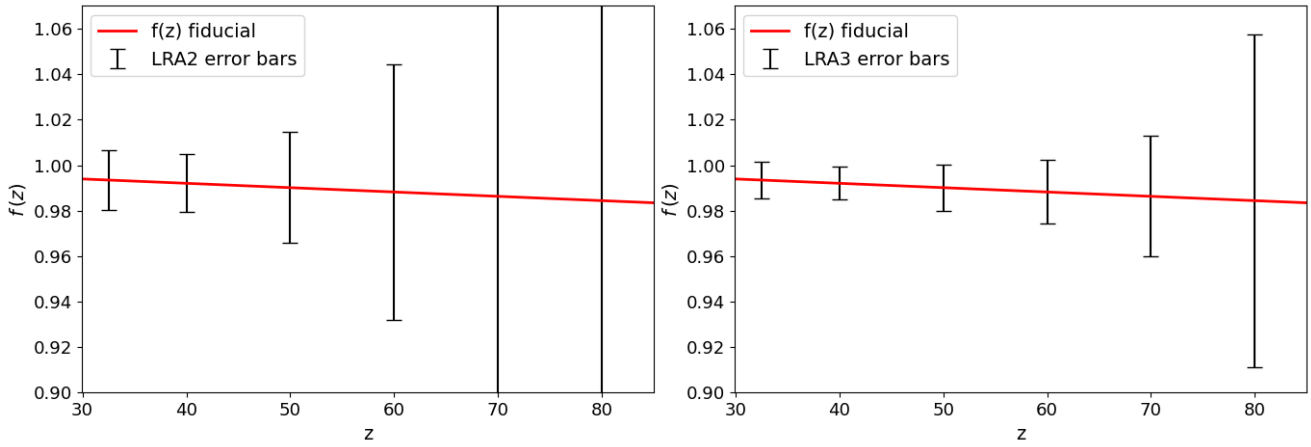

Figure 5.4: 68% confidence level constraints on $f(z)$ for LRA2 (left) and LRA3 (right), obtained from the combination of multiple redshift bins.

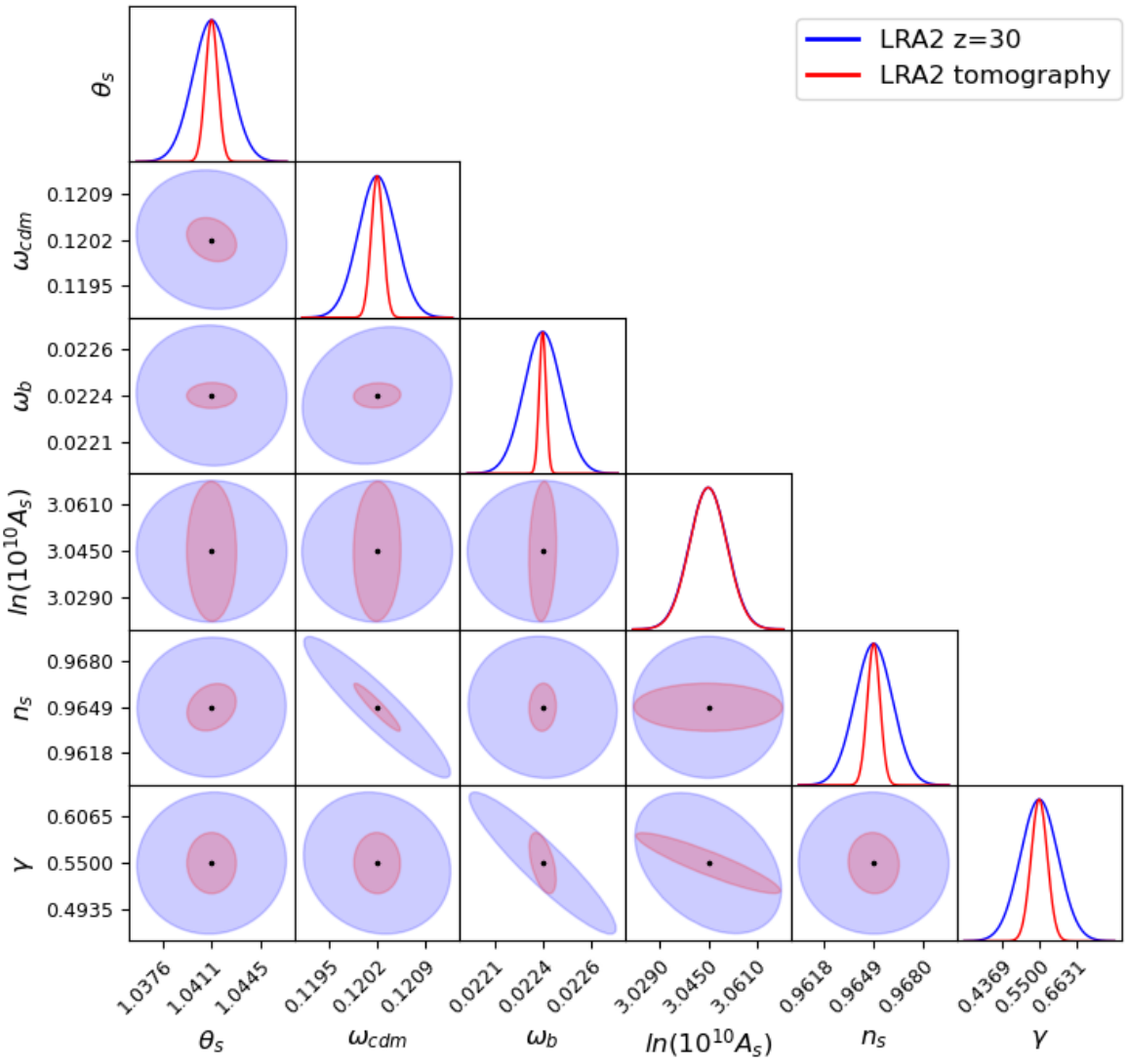

Figure 5.5: Two-dimensional 68% (1σ) confidence regions around the fiducial parameters forecasted for LRA2 measuring on a single redshift bin at $z = 30$ or in tomography in the range $30 < z < 200$.

correlation coefficient between the two, defined as in [75], decreases from $\rho = -0.92$ to $\rho = -0.52$ for LRA2 and from $\rho = -0.78$ to $\rho = -0.50$ for LRA3 when using tomography. There is no improvement in the case of LRA1, for which the correlation coefficients remains fixed at $\rho = -0.99$. The degeneracy between the parameters $\gamma - \omega_{\rm cdm}$ and $\omega_{\rm cdm} - \omega_b$, even if smaller to begin with, is also reduced with tomography for LRA2 and LRA3. An exception to this behavior is constituted by the parameter combination n_s and $\omega_{\rm cdm}$, which are highly anti-correlated ($|\rho| > 0.9$) for all the analyzed cases.

Most modified gravity models predict a time-varying growth index. In order to determine how well LIM experiments targeting the 21 cm signal from the Dark Ages will be able to detect the time variation of the growth index, we use the parametrization

$$\gamma(z) = \gamma_0 + \gamma_1 \frac{z}{1+z} \tag{5.9}$$

where γ_0 and γ_1 are constant. As in the previous case, we adopt the ΛCDM+GR values, $\gamma_0 = 0.55$ and $\gamma_1 = 0$, as fiducial. The marginalized constraints forecasted on these two parameters for all cases analyzed previously for constant γ are reported in Table 5.3.

Once we account for the possible time-variation of the growth index, the constraints on it become weaker by 1 - 3 orders of magnitude with respect to the case with constant γ. The absolute error found on γ_0 and γ_1 is similar for all cases.

We find that a time-varying growth index cannot be constrained with observations from Earth, even with a large instrument like aSKA. Precision constraints on γ_0 and γ_1 can be achieved only through tomographic analysis with LRA2 and LRA3. Using tomography improves the constraints on γ_0 and γ_1 by about 2 orders of magnitude for all configurations of LRA. Differently from the case with constant γ, LRA1 preforms better than aSKA when using tomography, with an improvement on the constraints by a factor ~ 2 for both parameters. Tomography with LRA2 and LRA3 will bring an improvement of 2-3 orders of magnitude on the aSKA constraints.

We conclude that, in this case, the determining factor on the precision of the constraints is the ability to perform tomography with a sufficient number of redshift bins for which the signal-to-noise is above one.

Experiment	z	$\sigma_{\gamma_0}/\gamma_0$	σ_{γ_1}
SKA	$z = 30$	1.45×10^6	8.26×10^5
aSKA	$z = 30$	58.5	33.3
LRA1	$z = 30$	2.39×10^3	1.36×10^3
	$30 < z < 200$	26.0	15.7
LRA2	$z = 30$	28.6	26.2
	$30 < z < 200$	2.67×10^{-1}	1.55×10^{-1}
LRA3	$z = 30$	7.21	4.05
	$30 < z < 200$	1.01×10^{-1}	4.20×10^{-2}

Table 5.5: Marginalized 68% C.L. constraints on the growth index amplitude and time variation, forecasted for each configuration of SKA and LRA. We report the relative error for γ_0 and the absolute error for γ_1.

As expected, γ_0 and γ_1 are completely degenerate for observations at a single redshift bin. In figure 5.6 (left) we report the 68% confidence region for the two parameters for observations with LRA2 at $z = 30$ and for tomographic analysis over the redshift range $30 < z < 200$. From the result it is clear that the degeneracy is reduced substantially when using tomography. We find similar results for the other configurations of LRA, not shown here.

The anti-correlation between γ_0 and γ_1 decreases as the number of redshift bins for which $S/N > 1$ increases. In Figure 5.6 (right) we compare the 68% confidence region for γ_0 and γ_1, forecasted for tomography with LRA2 and LRA3, where we indeed see this behaviour. This trend is also confirmed by the results that we obtain for LRA1.

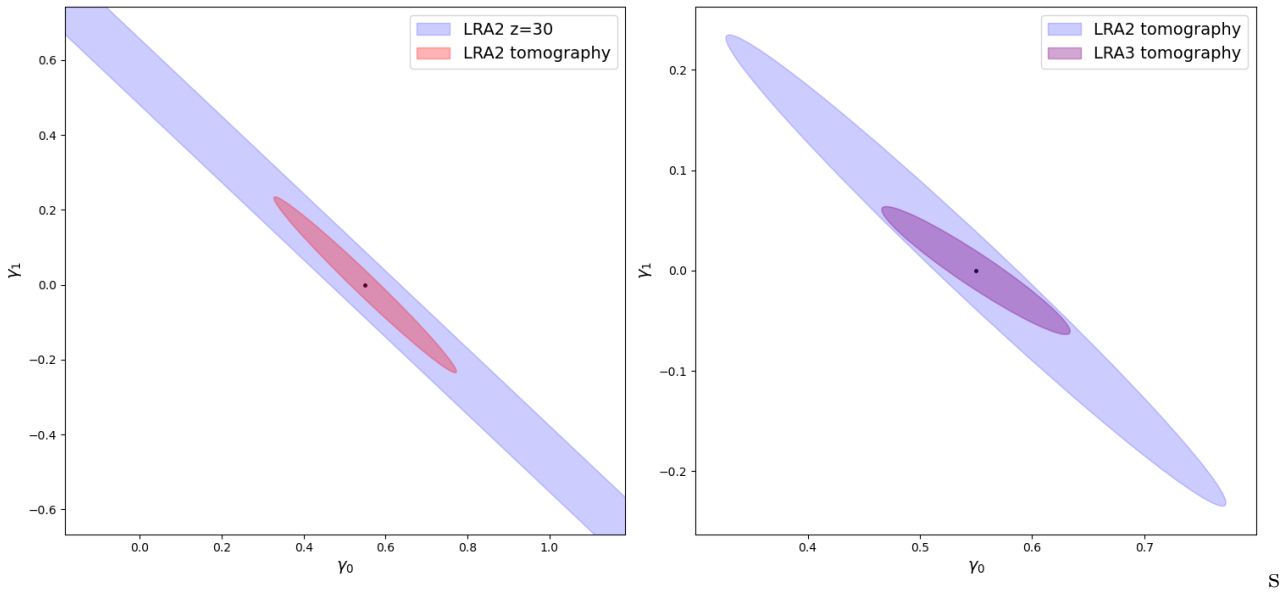

Figure 5.6: Two-dimensional 68% (1σ) confidence region for the parameters γ_0 and γ_1, forecasted for observations at a single redshift bin at $z = 30$ and for tomography with LRA2 (left) and for tomography with LRA2 and LRA3 (right).

Chapter 6

Conclusions

Understanding the nature of cosmic acceleration is one of the main challenges of modern cosmology and fundamental physics. In this work we consider the possibility that the accelerated expansion of the universe originates from the fact that General Relativity ceases to be a valid description of gravity on scales that are large with respect to the Solar System, where GR has been tested to high precision by numerous experiments.
Line Intensity Mapping is an optimal technique to access large scales and high redshifts that are out of reach for other probes, therefore it has great potential for cosmological tests of gravity.

Motivated by the recent development and future prospects of LIM, we aimed to study the potential of future intensity mapping experiments targeting the 21 cm emission line of neutral hydrogen to constrain the growth of matter density fluctuations during the Dark Ages, in the redshift range $30 < z < 200$, and detect any deviations from General Relativity. We considered different configurations for the upcoming ground-based radio interferometer SKA and for the proposed radio array on the far side of the Moon.
We forecast constraints on the growth of structure with the Fisher analysis, both by adopting the growth index parametrization for the growth rate of matter density fluctuations and by constraining the growth rate directly, treating it as a free redshift-dependent step function. In doing so we choose not to assume any specific modified gravity model and take the ΛCDM+GR values for the growth index and growth rate as fiducial.

According to our forecast, SKA won't be able to constrain cosmological parameters during Dark Ages. We find that, in order to achieve precision constraints on the growth index and the growth rate, the baseline of the interferometer needs to be of order ~ 100 km or larger. Following this requirement, a ground-base interferometer could already provide $\sim 10\%$ precision constraints, which are comparable with the best currently available measures at low redshifts. However, observations of the 21 cm line emission from Earth are limited to $z \leq 30$ due to the presence of the atmosphere.

Lunar-based observations would allow to measure the 21 cm brightness temperature over the entirety of the Dark Ages. The additional information from higher redshifts brought by tomographic analysis improves the constraints on the growth index by a factor 4 - 5 with respect to observations at $z = 30$ only, reaching a precision of $3 - 5\%$. The ability to access higher redshifts is fundamental when constraining the variation in time of the growth index, for which the error improves by 2 - 3 orders of magnitude. An additional advantage of observations from the far side of the Moon is the possibility to constrain the redshift evolution of the growth rate with precision level below 10% in the range $30 < z < 80$ and achieve sub-percent precision towards the end of the Dark Ages when combining multiple redshift bins. At last, we found that tomography reduces the degeneracy between parameters.

We conclude that 21 cm LIM experiments have the potential to achieve precision constraints on the growth of structure and test gravity on cosmological scales. In fact, radio interferometers currently operational or under construction, including SKA in the configuration examined in this work, won't be able to detect the 21 cm angular power spectrum from the Dark Ages with $S/N > 1$. A more

advanced instrument with baseline at least ~ 10 times larger and much better sensitivity is needed in order to achieve this goal and shed more light on the mechanism driving cosmic acceleration and improve our understanding on gravity. The advanced version of SKA studied in this work already satisfies these requirements, but it's only with observations from the far side of the Moon that the full information contained in the 21 cm signal from the Dark Ages would be exploited.

Bibliography

[1] N. Aghanim et al. "Planck 2018 results. VI. Cosmological parameters". In: *Astron. Astrophys.* 641 (2020). [Erratum: Astron.Astrophys. 652, C4 (2021)], A6. DOI: 10.1051/0004-6361/201833910. arXiv: 1807.06209 [astro-ph.CO].

[2] L. Guzzo et al. "Measuring the Universe with galaxy redshift surveys". In: *Congress of the Department of Physics Aldo Pontremoli*. Cham: Springer, 2018, pp. 1–16. DOI: 10.1007/978-3-030-01629-6_1. arXiv: 1803.10814 [astro-ph.CO].

[3] Shadab Alam et al. "Completed SDSS-IV extended Baryon Oscillation Spectroscopic Survey: Cosmological implications from two decades of spectroscopic surveys at the Apache Point Observatory". In: *Phys. Rev. D* 103.8 (2021), p. 083533. DOI: 10.1103/PhysRevD.103.083533. arXiv: 2007.08991 [astro-ph.CO].

[4] Henry S. Grasshorn Gebhardt and Donghui Jeong. "Nonlinear redshift-space distortions in the harmonic-space galaxy power spectrum". In: *Phys. Rev. D* 102.8 (2020), p. 083521. DOI: 10.1103/PhysRevD.102.083521. arXiv: 2008.08706 [astro-ph.CO].

[5] Diego Blas, Julien Lesgourgues, and Thomas Tram. "The Cosmic Linear Anisotropy Solving System (CLASS) II: Approximation schemes". In: *JCAP* 07 (2011), p. 034. DOI: 10.1088/1475-7516/2011/07/034. arXiv: 1104.2933 [astro-ph.CO].

[6] Daniel J. Eisenstein and Wayne Hu. "Baryonic features in the matter transfer function". In: *Astrophys. J.* 496 (1998), p. 605. DOI: 10.1086/305424. arXiv: astro-ph/9709112.

[7] N. Aghanim et al. "Planck 2018 results. I. Overview and the cosmological legacy of Planck". In: *Astron. Astrophys.* 641 (2020), A1. DOI: 10.1051/0004-6361/201833880. arXiv: 1807.06205 [astro-ph.CO].

[8] Adam G. Riess et al. "Observational Evidence from Supernovae for an Accelerating Universe and a Cosmological Constant". In: 116.3 (Sept. 1998), pp. 1009–1038. DOI: 10.1086/300499. arXiv: astro-ph/9805201 [astro-ph].

[9] Steven Weinberg. "The Cosmological constant problems". In: *4th International Symposium on Sources and Detection of Dark Matter in the Universe (DM 2000)*. Feb. 2000, pp. 18–26. arXiv: astro-ph/0005265.

[10] H. E. S. Velten, R. F. vom Marttens, and W. Zimdahl. "Aspects of the cosmological "coincidence problem"". In: *Eur. Phys. J. C* 74.11 (2014), p. 3160. DOI: 10.1140/epjc/s10052-014-3160-4. arXiv: 1410.2509 [astro-ph.CO].

[11] Ivaylo Zlatev, Li-Min Wang, and Paul J. Steinhardt. "Quintessence, cosmic coincidence, and the cosmological constant". In: *Phys. Rev. Lett.* 82 (1999), pp. 896–899. DOI: 10.1103/PhysRevLett.82.896. arXiv: astro-ph/9807002.

[12] Sean M. Carroll. "Quintessence and the rest of the world". In: *Phys. Rev. Lett.* 81 (1998), pp. 3067–3070. DOI: 10.1103/PhysRevLett.81.3067. arXiv: astro-ph/9806099.

[13] Ely D. Kovetz et al. "Line-Intensity Mapping: 2017 Status Report". In: (Sept. 2017). arXiv: 1709.09066 [astro-ph.CO].

[14] David J. Bacon et al. "Cosmology with Phase 1 of the Square Kilometre Array: Red Book 2018: Technical specifications and performance forecasts". In: *Publ. Astron. Soc. Austral.* 37 (2020), e007. DOI: 10.1017/pasa.2019.51. arXiv: 1811.02743 [astro-ph.CO].

[15] José Luis Bernal et al. "User's guide to extracting cosmological information from line-intensity maps". In: *Phys. Rev. D* 100.12 (2019), p. 123522. DOI: 10.1103/PhysRevD.100.123522. arXiv: 1907.10067 [astro-ph.CO].

[16] Marta B. Silva et al. "Mapping large-scale-structure evolution over cosmic times". In: *Exper. Astron.* 51.3 (2021), pp. 1593–1622. DOI: 10.1007/s10686-021-09755-3. arXiv: 1908.07533 [astro-ph.CO].

[17] Yacine Ali-Haımoud, P. Daniel Meerburg, and Sihan Yuan. "New light on 21 cm intensity fluctuations from the dark ages". In: *Phys. Rev. D* 89.8 (2014), p. 083506. DOI: 10.1103/PhysRevD.89.083506. arXiv: 1312.4948 [astro-ph.CO].

[18] Jonathan R. Pritchard and Abraham Loeb. "21-cm cosmology". In: *Rept. Prog. Phys.* 75 (2012), p. 086901. DOI: 10.1088/0034-4885/75/8/086901. arXiv: 1109.6012 [astro-ph.CO].

[19] Steven Furlanetto, S. Peng Oh, and Frank Briggs. "Cosmology at Low Frequencies: The 21 cm Transition and the High-Redshift Universe". In: *Phys. Rept.* 433 (2006), pp. 181–301. DOI: 10.1016/j.physrep.2006.08.002. arXiv: astro-ph/0608032.

[20] George B. Field. "Excitation of the Hydrogen 21-CM Line". In: *Proceedings of the IRE* 46 (Jan. 1958), pp. 240–250. DOI: 10.1109/JRPROC.1958.286741.

[21] George B. Rybicki and Alan P. Lightman. *Radiative Processes in Astrophysics*. 1986.

[22] Abraham Loeb and Matias Zaldarriaga. "Measuring the small - scale power spectrum of cosmic density fluctuations through 21 cm tomography prior to the epoch of structure formation". In: *Phys. Rev. Lett.* 92 (2004), p. 211301. DOI: 10.1103/PhysRevLett.92.211301. arXiv: astro-ph/0312134.

[23] Michael Kuhlen, Piero Madau, and Ryan Montgomery. "The spin temperature and 21cm brightness of the intergalactic medium in the pre-reionization era". In: *Astrophys. J. Lett.* 637 (2006), pp. L1–L4. DOI: 10.1086/500548. arXiv: astro-ph/0510814.

[24] Steven Furlanetto. "The Global 21 Centimeter Background from High Redshifts". In: *Mon. Not. Roy. Astron. Soc.* 371 (2006), pp. 867–878. DOI: 10.1111/j.1365-2966.2006.10725.x. arXiv: astro-ph/0604040.

[25] Patrick C. Breysse, Yacine Ali-Haımoud, and Christopher M. Hirata. "Ultimate frontier of 21-cm cosmology". In: *Phys. Rev. D* 98.4 (2018), p. 043520. DOI: 10.1103/PhysRevD.98.043520. arXiv: 1804.10626 [astro-ph.CO].

[26] Antony Lewis and Anthony Challinor. "The 21cm angular-power spectrum from the dark ages". In: *Phys. Rev. D* 76 (2007), p. 083005. DOI: 10.1103/PhysRevD.76.083005. arXiv: astro-ph/0702600.

[27] Julian B. Muñoz, Yacine Ali-Haımoud, and Marc Kamionkowski. "Primordial non-gaussianity from the bispectrum of 21-cm fluctuations in the dark ages". In: *Phys. Rev. D* 92.8 (2015), p. 083508. DOI: 10.1103/PhysRevD.92.083508. arXiv: 1506.04152 [astro-ph.CO].

[28] Annalisa Pillepich, Cristiano Porciani, and Sabino Matarrese. "The bispectrum of redshifted 21-cm fluctuations from the dark ages". In: *Astrophys. J.* 662 (2007), pp. 1–14. DOI: 10.1086/517963. arXiv: astro-ph/0611126.

[29] Dmitriy Tseliakhovich and Christopher Hirata. "Relative velocity of dark matter and baryonic fluids and the formation of the first structures". In: *Phys. Rev. D* 82 (2010), p. 083520. DOI: 10.1103/PhysRevD.82.083520. arXiv: 1005.2416 [astro-ph.CO].

[30] Henry S. Grasshorn Gebhardt and Donghui Jeong. "Fast and accurate computation of projected two-point functions". In: *Phys. Rev. D* 97.2 (2018), p. 023504. DOI: 10.1103/PhysRevD.97.023504. arXiv: 1709.02401 [astro-ph.CO].

[31] Shinji Tsujikawa. "Modified gravity models of dark energy". In: *Lect. Notes Phys.* 800 (2010), pp. 99–145. DOI: 10.1007/978-3-642-10598-2_3. arXiv: 1101.0191 [gr-qc].

[32] Li-Min Wang and Paul J. Steinhardt. "Cluster abundance constraints on quintessence models". In: *Astrophys. J.* 508 (1998), pp. 483–490. DOI: 10.1086/306436. arXiv: astro-ph/9804015.

[33] Eric V. Linder. "Cosmic growth history and expansion history". In: *Phys. Rev. D* 72 (2005), p. 043529. DOI: 10.1103/PhysRevD.72.043529. arXiv: astro-ph/0507263.

[34] P. A. R. Ade et al. "Planck 2015 results. XIV. Dark energy and modified gravity". In: *Astron. Astrophys.* 594 (2016), A14. DOI: 10.1051/0004-6361/201525814. arXiv: 1502.01590 [astro-ph.CO].

[35] Eric V. Linder and Robert N. Cahn. "Parameterized Beyond-Einstein Growth". In: *Astropart. Phys.* 28 (2007), pp. 481–488. DOI: 10.1016/j.astropartphys.2007.09.003. arXiv: astro-ph/0701317.

[36] Khaled Said et al. "Joint analysis of 6dFGS and SDSS peculiar velocities for the growth rate of cosmic structure and tests of gravity". In: *Mon. Not. Roy. Astron. Soc.* 497.1 (2020), pp. 1275–1293. DOI: 10.1093/mnras/staa2032. arXiv: 2007.04993 [astro-ph.CO].

[37] Nick Kaiser. "Clustering in real space and in redshift space". In: 227 (July 1987), pp. 1–21. DOI: 10.1093/mnras/227.1.1.

[38] Alvise Raccanelli, Lado Samushia, and Will J. Percival. "Simulating Redshift-Space Distortions for Galaxy Pairs with Wide Angular Separation". In: *Mon. Not. Roy. Astron. Soc.* 409 (2010), p. 1525. DOI: 10.1111/j.1365-2966.2010.17388.x. arXiv: 1006.1652 [astro-ph.CO].

[39] Felipe Avila et al. "Inferring $S_8(z)$ and $\gamma(z)$ with cosmic growth rate measurements using machine learning". In: *Eur. Phys. J. C* 82.7 (2022), p. 594. DOI: 10.1140/epjc/s10052-022-10561-0. arXiv: 2201.07829 [astro-ph.CO].

[40] Michael J. Hudson and Stephen J. Turnbull. "The growth rate of cosmic structure from peculiar velocities at low and high redshifts". In: *Astrophys. J. Lett.* 751 (2013), p. L30. DOI: 10.1088/2041-8205/751/2/L30. arXiv: 1203.4814 [astro-ph.CO].

[41] D. M. Scolnic et al. "The Complete Light-curve Sample of Spectroscopically Confirmed SNe Ia from Pan-STARRS1 and Cosmological Constraints from the Combined Pantheon Sample". In: *Astrophys. J.* 859.2 (2018), p. 101. DOI: 10.3847/1538-4357/aab9bb. arXiv: 1710.00845 [astro-ph.CO].

[42] Thomas L. Wilson, Kristen Rohlfs, and Susanne Hüttemeister. *Tools of Radio Astronomy*. 2009. DOI: 10.1007/978-3-540-85122-6.

[43] David J. Bacon et al. "Cosmology with Phase 1 of the Square Kilometre Array: Red Book 2018: Technical specifications and performance forecasts". In: *Publ. Astron. Soc. Austral.* 37 (2020), e007. DOI: 10.1017/pasa.2019.51. arXiv: 1811.02743 [astro-ph.CO].

[44] Adrian Liu and J. Richard Shaw. "Data Analysis for Precision 21 cm Cosmology". In: *Publ. Astron. Soc. Pac.* 132.1012 (2020), p. 062001. DOI: 10.1088/1538-3873/ab5bfd. arXiv: 1907.08211 [astro-ph.IM].

[45] Ue-Li Pen et al. "First Detection of Cosmic Structure in the 21-cm Intensity Field". In: *Mon. Not. Roy. Astron. Soc.* 394 (2009), p. 6. DOI: 10.1111/j.1745-3933.2008.00581.x. arXiv: 0802.3239 [astro-ph].

[46] Tzu-Ching Chang et al. "Hydrogen 21-cm Intensity Mapping at redshift 0.8". In: *Nature* 466 (2010), pp. 463–465. DOI: 10.1038/nature09187. arXiv: 1007.3709 [astro-ph.CO].

[47] Mandana Amiri et al. "Detection of Cosmological 21 cm Emission with the Canadian Hydrogen Intensity Mapping Experiment". In: (Feb. 2022). arXiv: 2202.01242 [astro-ph.CO].

[48] Laura Wolz et al. "H I constraints from the cross-correlation of eBOSS galaxies and Green Bank Telescope intensity maps". In: *Mon. Not. Roy. Astron. Soc.* 510.3 (2022), pp. 3495–3511. DOI: 10.1093/mnras/stab3621. arXiv: 2102.04946 [astro-ph.CO].

[49] Hamsa Padmanabhan, T. Roy Choudhury, and Alexandre Refregier. "Theoretical and observational constraints on the HI intensity power spectrum". In: *Mon. Not. Roy. Astron. Soc.* 447 (2015), p. 3745. DOI: 10.1093/mnras/stu2702. arXiv: 1407.6366 [astro-ph.CO].

[50] B. K. Gehlot et al. "The first power spectrum limit on the 21-cm signal of neutral hydrogen during the Cosmic Dawn at z = 20-25 from LOFAR". In: 488.3 (2019), pp. 4271–4287. DOI: 10.1093/mnras/stz1937. arXiv: 1809.06661 [astro-ph.IM].

[51] Andrei Mesinger, Bradley Greig, and Emanuele Sobacchi. "The Evolution Of 21 cm Structure (EOS): public, large-scale simulations of Cosmic Dawn and reionization". In: *Mon. Not. Roy. Astron. Soc.* 459.3 (2016), pp. 2342–2353. DOI: 10.1093/mnras/stw831. arXiv: 1602.07711 [astro-ph.CO].

[52] Zara Abdurashidova et al. "First Results from HERA Phase I: Upper Limits on the Epoch of Reionization 21 cm Power Spectrum". In: *Astrophys. J.* 925.2 (2022), p. 221. DOI: 10.3847/1538-4357/ac1c78. arXiv: 2108.02263 [astro-ph.CO].

[53] Nichole Barry et al. "SKA-low intensity mapping pathfinder updates: deeper 21 cm power spectrum limits from improved analysis frameworks". In: *J. Astron. Telesc. Instrum. Syst.* 8.1 (2021), p. 011007. DOI: 10.1117/1.JATIS.8.1.011007. arXiv: 2110.06173 [astro-ph.CO].

[54] Judd D. Bowman et al. "An absorption profile centred at 78 megahertz in the sky-averaged spectrum". In: *Nature* 555.7694 (2018), pp. 67–70. DOI: 10.1038/nature25792. arXiv: 1810.05912 [astro-ph.CO].

[55] Aviad Cohen, Anastasia Fialkov, and Rennan Barkana. "Charting the Parameter Space of the 21-cm Power Spectrum". In: *Mon. Not. Roy. Astron. Soc.* 478.2 (2018), pp. 2193–2217. DOI: 10.1093/mnras/sty1094. arXiv: 1709.02122 [astro-ph.CO].

[56] José Luis Bernal, Patrick C. Breysse, and Ely D. Kovetz. "Cosmic Expansion History from Line-Intensity Mapping". In: *Phys. Rev. Lett.* 123.25 (2019), p. 251301. DOI: 10.1103/PhysRevLett.123.251301. arXiv: 1907.10065 [astro-ph.CO].

[57] A. Weltman et al. "Fundamental physics with the Square Kilometre Array". In: *Publ. Astron. Soc. Austral.* 37 (2020), e002. DOI: 10.1017/pasa.2019.42. arXiv: 1810.02680 [astro-ph.CO].

[58] Adam G. Riess et al. "Large Magellanic Cloud Cepheid Standards Provide a 1% Foundation for the Determination of the Hubble Constant and Stronger Evidence for Physics beyond ΛCDM". In: *Astrophys. J.* 876.1 (2019), p. 85. DOI: 10.3847/1538-4357/ab1422. arXiv: 1903.07603 [astro-ph.CO].

[59] Marco Raveri et al. "Priors on the effective Dark Energy equation of state in scalar-tensor theories". In: *Phys. Rev. D* 96.8 (2017), p. 083509. DOI: 10.1103/PhysRevD.96.083509. arXiv: 1703.05297 [astro-ph.CO].

[60] Katie Short et al. "Enlightening the dark ages with dark matter". In: *JCAP* 07 (2020), p. 020. DOI: 10.1088/1475-7516/2020/07/020. arXiv: 1912.07409 [astro-ph.CO].

[61] Julian B. Muñoz, Ely D. Kovetz, and Yacine Ali-Haımoud. "Heating of Baryons due to Scattering with Dark Matter During the Dark Ages". In: *Phys. Rev. D* 92.8 (2015), p. 083528. DOI: 10.1103/PhysRevD.92.083528. arXiv: 1509.00029 [astro-ph.CO].

[62] Alvise Raccanelli et al. "Detecting the integrated Sachs-Wolfe effect with high-redshift 21-cm surveys". In: *Phys. Rev. D* 93.8 (2016), p. 083512. DOI: 10.1103/PhysRevD.93.083512. arXiv: 1502.03107 [astro-ph.CO].

[63] David Alonso et al. "Calibrating photometric redshifts with intensity mapping observations". In: *Phys. Rev. D* 96.4 (2017), p. 043515. DOI: 10.1103/PhysRevD.96.043515. arXiv: 1704.01941 [astro-ph.CO].

[64] Ely D. Kovetz, Alvise Raccanelli, and Mubdi Rahman. "Cosmological Constraints with Clustering-Based Redshifts". In: *Mon. Not. Roy. Astron. Soc.* 468.3 (2017), pp. 3650–3656. DOI: 10.1093/mnras/stx691. arXiv: 1606.07434 [astro-ph.CO].

[65] Léon V. E. Koopmans et al. "Peering into the dark (ages) with low-frequency space interferometers: Using the 21-cm signal of neutral hydrogen from the infant universe to probe fundamental (Astro)physics". In: *Exper. Astron.* 51.3 (2021), pp. 1641–1676. DOI: 10.1007/s10686-021-09743-7. arXiv: 1908.04296 [astro-ph.IM].

[66] Jack Burns et al. "A Lunar Farside Low Radio Frequency Array for Dark Ages 21-cm Cosmology". In: (Mar. 2021). arXiv: 2103.08623 [astro-ph.IM].

[67] Patrick McGarey et al. "How to Deploy a 10-km Interferometric Radio Telescope on the Moon with Just Four Tethered Robots". In: *2022 IEEE Aerospace Conference (AERO)*. 2022, pp. 1–8. DOI: 10.1109/AERO53065.2022.9843745.

[68] Elimboto Yohana, Yi-Chao Li, and Yin-Zhe Ma. "Forecasts of cosmological constraints from HI intensity mapping with FAST, BINGO & SKA-I". In: (Aug. 2019). DOI: 10.1088/1674-4527/19/12/186. arXiv: 1908.03024 [astro-ph.CO].

[69] Arthur Loureiro et al. "Cosmological measurements from angular power spectra analysis of BOSS DR12 tomography". In: *Mon. Not. Roy. Astron. Soc.* 485.1 (2019), pp. 326–355. DOI: 10.1093/mnras/stz191. arXiv: 1809.07204 [astro-ph.CO].

[70] C. Alcock and B. Paczynski. "An evolution free test for non-zero cosmological constant". In: *Nature* 281 (1979), pp. 358–359. DOI: 10.1038/281358a0.

[71] Max Tegmark, Andy Taylor, and Alan Heavens. "Karhunen-Loeve eigenvalue problems in cosmology: How should we tackle large data sets?" In: *Astrophys. J.* 480 (1997), p. 22. DOI: 10.1086/303939. arXiv: astro-ph/9603021.

[72] Nicola Bellomo et al. "Beware of commonly used approximations. Part I. Errors in forecasts". In: *JCAP* 10 (2020), p. 016. DOI: 10.1088/1475-7516/2020/10/016. arXiv: 2005.10384 [astro-ph.CO].

[73] Matias Zaldarriaga, Steven R. Furlanetto, and Lars Hernquist. "21 Centimeter fluctuations from cosmic gas at high redshifts". In: *Astrophys. J.* 608 (2004), pp. 622–635. DOI: 10.1086/386327. arXiv: astro-ph/0311514.

[74] T. J. Mozdzen et al. "Improved measurement of the spectral index of the diffuse radio background between 90 and 190 MHz". In: 464.4 (Feb. 2017), pp. 4995–5002. DOI: 10.1093/mnras/stw2696. arXiv: 1609.08705 [astro-ph.IM].

[75] Dan Coe. "Fisher Matrices and Confidence Ellipses: A Quick-Start Guide and Software". In: (June 2009). arXiv: 0906.4123 [astro-ph.IM].